

## NEUROSCIENCE

# Functional specialization of different PI3K isoforms for the control of neuronal architecture, synaptic plasticity, and cognition

Carla Sánchez-Castillo<sup>1†‡</sup>, María I. Cuartero<sup>1‡§||</sup>, Alba Fernández-Rodrigo<sup>1</sup>, Víctor Briz<sup>1</sup>, Sergio López-García<sup>1</sup>, Raquel Jiménez-Sánchez<sup>1</sup>, Juan A. López<sup>2,3</sup>, Mariona Graupera<sup>4,5</sup>, José A. Esteban<sup>1\*</sup>

Neuronal connectivity and activity-dependent synaptic plasticity are fundamental properties that support brain function and cognitive performance. Phosphatidylinositol 3-kinase (PI3K) intracellular signaling controls multiple mechanisms mediating neuronal growth, synaptic structure, and plasticity. However, it is still unclear how these pleiotropic functions are integrated at molecular and cellular levels. To address this issue, we used neuron-specific virally delivered Cre expression to delete either p110 $\alpha$  or p110 $\beta$  (the two major catalytic isoforms of type I PI3K) from the hippocampus of adult mice. We found that dendritic and postsynaptic structures are almost exclusively supported by p110 $\alpha$  activity, whereas p110 $\beta$  controls neurotransmitter release and metabotropic glutamate receptor–dependent long-term depression at the presynaptic terminal. In addition to these separate functions, p110 $\alpha$  and p110 $\beta$  jointly contribute to *N*-methyl-D-aspartate receptor–dependent postsynaptic long-term potentiation. This molecular and functional specialization is reflected in different proteomes controlled by each isoform and in distinct behavioral alterations for learning/memory and sociability in mice lacking p110 $\alpha$  or p110 $\beta$ .

## INTRODUCTION

The experience-dependent modification of synaptic connections, known as synaptic plasticity, is considered the cellular basis for learning and memory (1, 2). The molecular mechanisms mediating these synaptic changes are still being elucidated, but it is becoming increasingly clear that neurons recruit common intracellular trafficking machinery and signaling pathways for these highly specialized processes. In particular, it is intriguing that synaptic plasticity and cellular growth/survival often rely on common signaling drivers (3). This is best exemplified by phosphatidylinositol 3-kinase (PI3K)/phosphatase and tensin homolog (PTEN) signaling: While PI3K activity is generally associated with synaptic potentiation and cellular growth, PTEN is linked to synaptic depression and growth restriction (4–11). However, this relation is far from univocal. Thus, it is well established that signaling through PI3Ks is a key mechanism mediating long-term potentiation (LTP) induced by *N*-methyl-D-aspartate (NMDA) receptors (NMDARs) (12–16). However, PI3K has also been associated with long-term depression

(LTD), most consistently when induced by metabotropic glutamate receptors (mGluRs) (17–19) and by NMDARs (20, 21). Together with these established roles in synaptic plasticity, the PI3K pathway drives neuronal growth and structural plasticity during synaptogenesis and neuronal development, exerting direct effects on dendritic complexity, spine number, and shape (22–29).

These pleiotropic (and sometimes antagonistic) effects driven by PI3K activity are possibly related to the molecular diversity of PI3Ks. Class IA PI3Ks are heterodimers consisting of a regulatory subunit (usually p85 $\alpha$  or p85 $\beta$ ) and a catalytic subunit (p110 $\alpha$ , p110 $\beta$ , or p110 $\delta$ ) that catalyzes the production of phosphatidylinositol 3,4,5-trisphosphate (PIP<sub>3</sub>) in response to ligand stimulation (30, 31). Some isoform-specific functions of PI3Ks are starting to be uncovered by means of gene-targeting approaches and from genetic data on human pathologies (32–35). Nevertheless, at this moment, the specific roles of individual PI3K isoforms in synaptic plasticity and neuronal morphology are largely unknown, as all PI3K isoforms are expressed in the brain, particularly in neurons. This is not only an academic issue. The knowledge of specific PI3K isoforms engaged for distinct neuronal functions will not only help to understand the regulatory mechanisms involved but may also provide more specific targets for certain pathological conditions.

Among class IA PI3K catalytic subunits, p110 $\alpha$  and p110 $\beta$  are ubiquitously expressed, and their absence results in embryonic lethality (36, 37). In neurons, these isoforms are well expressed throughout life. Therefore, we hypothesized that p110 $\alpha$  and p110 $\beta$  isoforms could have nonredundant roles in mature neurons regarding neuronal architecture, synaptic plasticity, and ultimately cognitive function. To bypass embryonic lethality, we have used a conditional and region-restricted gene-targeting approach, in combination with proteomic, imaging, electrophysiological,

<sup>1</sup>Department of Molecular Neuropathology, Centro de Biología Molecular Severo Ochoa (CSIC-UAM), Madrid, Spain. <sup>2</sup>Proteomics Unit, Centro Nacional de Investigaciones Cardiovasculares Carlos III (CNIC), Madrid, Spain. <sup>3</sup>Centro de Investigación Biomédica en Red de Enfermedades Cardiovasculares (CIBERCV), Instituto de Salud Carlos III, Madrid, Spain. <sup>4</sup>Endothelial Pathobiology and Microenvironment Group, Josep Carreras Leukaemia Research Institute (LJC), 08916 Badalona, Barcelona, Spain. <sup>5</sup>Centro de Investigación Biomédica en Red de Cáncer (CIBERONC), Instituto de Salud Carlos III, Madrid, Spain.

\*Corresponding author. Email: jaesteban@cbm.csic.es

†Present address: Department of Physiology, Genetics, and Microbiology, University of Alicante, Alicante, Spain.

‡These authors contributed equally to this work.

§Present address: Neurovascular Research Unit, Department of Pharmacology and Toxicology, Medical School at the Universidad Complutense de Madrid, Madrid, Spain.

||Present address: Neurovascular Pathophysiology Group, Centro Nacional de Investigaciones Cardiovasculares Carlos III (CNIC), Madrid, Spain.

and behavioral assays. On the basis of these experiments, we now report that neuronal ablation of p110 $\alpha$  or p110 $\beta$  differentially affects protein expression profiles, suggesting that both isoforms have separate functions in neurons. p110 $\alpha$  and p110 $\beta$  have different roles in synapse and dendritic maintenance, basal synaptic transmission, and synaptic plasticity. Last, mice lacking p110 $\alpha$  or p110 $\beta$  in the adult hippocampus exhibit distinct behavioral phenotypes in memory and social behavior.

## RESULTS

### Proteomic analyses of mice lacking neuronal p110 $\alpha$ or p110 $\beta$ evidence differential cellular processes controlled by the two isoforms

As mentioned above, PI3K signaling controls a variety of neuronal functions, including cell survival, neural circuit development, and synaptic plasticity (12–15, 17, 26). To get some insight into potentially different functions of the catalytic isoforms p110 $\alpha$  and p110 $\beta$ , we used a gene-targeting approach using Cre-lox recombination. To bypass the embryonic lethality of the complete knockout of *PIK3CA* and *PIK3CB* genes (36, 37), we bilaterally injected adeno-associated viruses (AAVs) expressing Cre recombinase under the calcium/calmodulin-dependent protein kinase II $\alpha$  (CaMKII $\alpha$ ) promoter (AAV5-CaMKII $\alpha$ -mCherry-Cre) into the hippocampus of adult p110 $\alpha^{lox/lox}$  and p110 $\beta^{lox/lox}$  mice (fig. S1A). Four weeks after injection, Cre was expressed mainly in neurons along the whole septotemporal axis of the hippocampus (38) with around 90% infection efficiency in dorsal and ventral CA1 neurons (fig. S1, B to E). As expected, the resulting neuronal p110 $\alpha$  and p110 $\beta$  knockout mice (p110 $\alpha^{nKO}$  and p110 $\beta^{nKO}$ , respectively) displayed a selective reduction in the p110 $\alpha$  and p110 $\beta$  protein levels of more than 50% (fig. S2, A and B). To note, the knockout efficiency is not expected to be 100% as p110 $\alpha$  and p110 $\beta$  are ubiquitously expressed and are expected to be present in glial cells and cerebral vasculature (39, 40). In both cases, downstream targets of the PI3K pathway seemed to be mostly unaltered (except for S6 expression in p110 $\alpha^{nKO}$ ; fig. S2, C to E).

To start investigating the cellular programs that may be specifically affected by p110 $\alpha$  or p110 $\beta$  deficiency, we performed tandem mass tagging (TMT)-based quantitative proteomic analysis to identify hippocampal proteins whose levels were altered in p110 $\alpha^{nKO}$  and p110 $\beta^{nKO}$  mice (Fig. 1 and fig. S3). Of the total of 7888 proteins identified, we found 1710 differentially expressed proteins (DEPs) between our three experimental conditions (p110 $\alpha^{nKO}$ , p110 $\beta^{nKO}$ , and wild-type mice infected with the same AAV; three animals per genotype). From these, 1040 DEPs arise from comparing p110 $\beta^{nKO}$  versus p110 $\alpha^{nKO}$  proteomic profiles, 395 correspond to p110 $\alpha^{nKO}$  versus control, and 275 correspond to p110 $\beta^{nKO}$  versus control (Fig. 1A and data S1). Some of these DEPs are unique to each comparison, and others are common as depicted by the numbers on the intersections of the Venn diagram. Pairwise comparison of DEPs across individual animals (Fig. 1B) showed high correlation coefficients in the replicates from both p110 $\alpha^{nKO}$  and p110 $\beta^{nKO}$ , indicating high reproducibility among the three replicates (and substantial differences across the three groups). p110 $\alpha^{nKO}$ , p110 $\beta^{nKO}$ , and control replicates clustered together by hierarchical clustering of all DEPs (Fig. 1C). Gene Ontology (GO) enrichment analysis for the proteins comprising each cluster identified as the top GO biological processes: actin filament organization, translation, cellular

localization, adenosine 5'-triphosphate (ATP) synthesis-coupled proton transport, cytoskeleton organization, and nervous system development (Fig. 1C). For most of the clusters (except for ATP synthesis), lack of p110 $\alpha$  and p110 $\beta$  had opposite effects. The absence of p110 $\alpha$  on pyramidal neurons seems to down-regulate actin cytoskeleton and translation-related proteins while promoting an increase in proteins involved in cellular localization and nervous system development. Conversely, deletion of p110 $\beta$  most notably decreased expression of proteins related to cellular localization and neuronal system development.

To further explore the cellular processes and pathways most affected by the absence of p110 $\alpha$  and p110 $\beta$ , we performed an enrichment analysis (Fig. 1D). From the comparison of the 1040 DEPs between p110 $\alpha^{nKO}$  and p110 $\beta^{nKO}$ , we found several categories in both biological and cellular components that exhibited marked changes between PI3K isoforms. Notably, the most remarkable differences were found in actin cytoskeleton and organization and filament polymerization, dendrite development and synapse organization, as well as postsynaptic and dendritic components. In addition, we found several presynaptic proteins (synaptic vesicle glycoprotein 2B [SV2B] and vesicle-associated membrane protein 7 [VAMP7]) up-regulated in p110 $\beta^{nKO}$  and postsynaptic and structural proteins (PSD95, CaMKII $\alpha$ , AMPA receptor subunit 2 [GluA2],  $\alpha$ -actinin-1, and microtubule-associated protein 2 [MAP2]) down-regulated in p110 $\alpha^{nKO}$  (Fig. 1E). These results already point out to p110 $\alpha$  and p110 $\beta$  as important (and differing) master regulators of synaptic and neuronal structure.

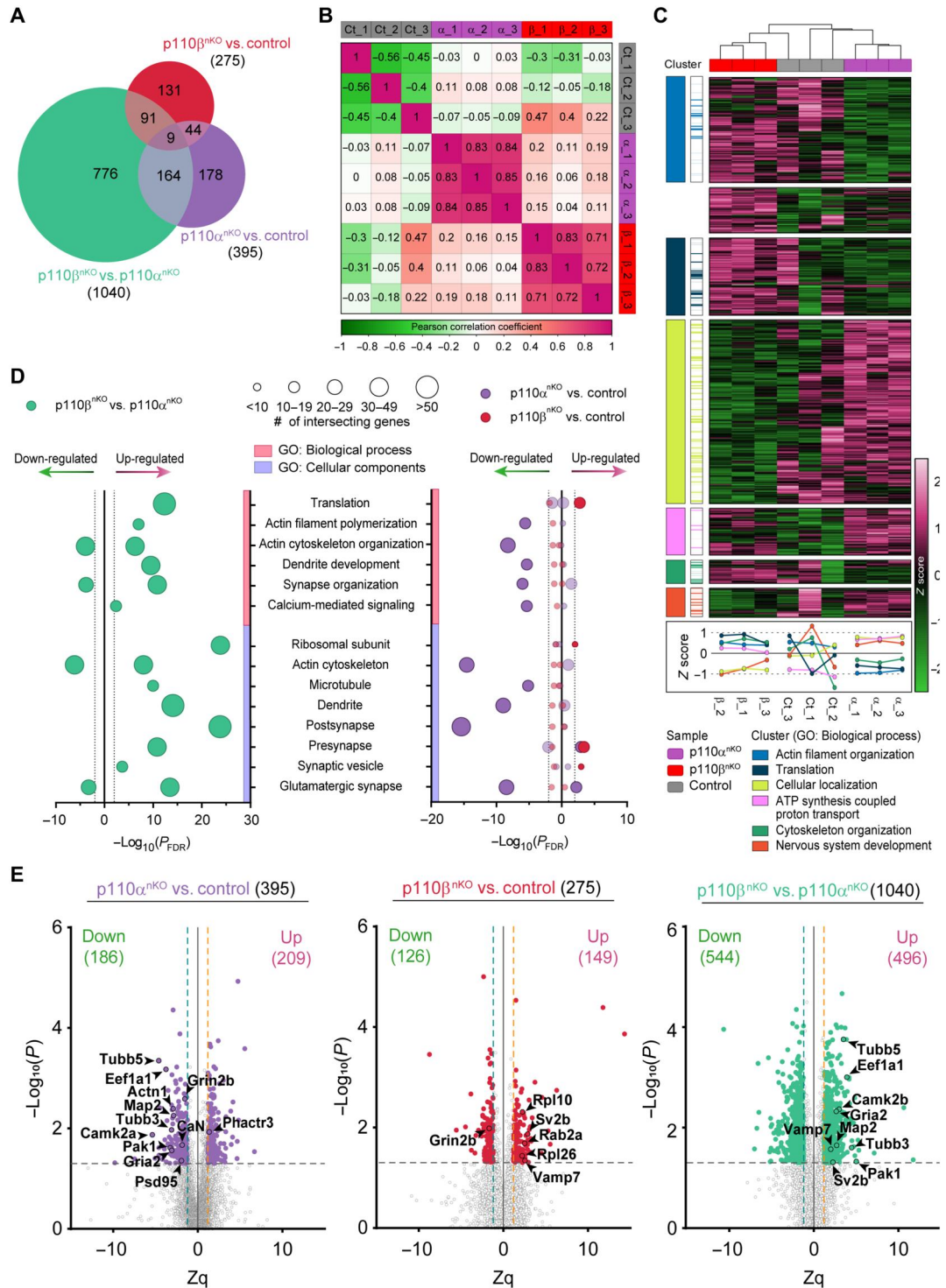
Last, the differential expression profiles caused by neuronal deletion of p110 $\alpha$  and p110 $\beta$  were further evaluated by Western blot (fig. S4). We found that AMPA receptor (AMPA) and NMDAR subunits were significantly decreased in hippocampal lysates from both p110 $\alpha^{nKO}$  and p110 $\beta^{nKO}$ . The phosphorylation of cofilin was significantly increased solely in the case of p110 $\alpha^{nKO}$ , reinforcing the link between p110 $\alpha$  and the actin cytoskeleton. In addition, the levels of the Ca<sup>2+</sup>/calmodulin-dependent phosphatase calcineurin (CaN) and the phosphorylation of  $\alpha$ CaMKII were specifically affected by p110 $\beta$  deletion on pyramidal neurons. Therefore, together, these changes suggest that p110 $\alpha$  and p110 $\beta$  isoforms might play differential roles in synaptic function and intracellular signaling.

### Loss of p110 $\alpha$ but not p110 $\beta$ impairs dendritic and spine maintenance in hippocampal pyramidal neurons

Our previous proteomic data clearly pointed to proteins linked to the actin cytoskeleton, particularly in mice lacking p110 $\alpha$ . Therefore, we evaluated whether the absence of p110 $\alpha$  or p110 $\beta$  leads to structural or morphological hippocampal alterations. We first analyzed the hippocampal volume of p110 $\alpha^{nKO}$  and p110 $\beta^{nKO}$  by *ex vivo* magnetic resonance imaging approximately 1 month after hippocampal AAV delivery (Fig. 2, A to E, and fig. S5). Both p110 $\alpha^{nKO}$  and p110 $\beta^{nKO}$  mice displayed a significant reduction in hippocampal volume (Fig. 2, A to D), although this reduction was significantly more pronounced in p110 $\alpha^{nKO}$  as compared to p110 $\beta^{nKO}$  mice (33.8  $\pm$  3.4% of hippocampal volume loss in p110 $\alpha^{nKO}$  versus 16.4  $\pm$  2.7% in p110 $\beta^{nKO}$ ; Fig. 2E). To note, neither the volume of the hemispheres nor the cortex was altered in p110 $\alpha^{nKO}$  or p110 $\beta^{nKO}$  mice, supporting the specificity of the hippocampal AAV delivery (fig. S5, C, D, H, and I). These results

**Fig. 1. Proteomic analysis of mice lacking neuronal p110α or p110β.**

(A) Venn diagram of DEPs for all possible comparisons. (B) Similarity matrix showing pairwise distances between samples, measured by Pearson correlation. (C) Unsupervised hierarchical clustering based on Euclidean distances for the 1710 DEPs. Colors represent row-scaled expression values (green, low expression; magenta, high expression). Seven protein clusters were identified on the basis of their expression pattern, and GO biological process enrichment analysis was performed on each cluster. GO biological process terms are annotated for each cluster (left cluster panel), and the intersecting proteins from the dataset are highlighted with the same color code (right cluster panel). Clusters are also represented by sample expression levels in the panel below the heatmap. (D) GO enrichment analysis of the DEPs ( $|Zq| > 1.2$  and  $P < 0.05$ ) for p110β versus p110α (left plot) and for p110α and p110β versus control (right plot). For both plots, GO biological process and cell components are plotted against the adjusted  $P$  value by Benjamini-Hochberg false discovery rate ( $P_{FDR}$ ) correction ( $P_{FDR}$ ). Dotted lines represent significance threshold ( $P_{FDR} < 0.01$ ,  $|\log_{10}(P_{FDR})| > 2$ ) for all GO terms, and the size of the points represents the number of intersecting genes between the dataset and the GO biological process or the GO cell component. Sign on the  $x$  axis represents up- or down-regulation.  $n = 3$  mice per group. (E) Volcano plots of DEPs ( $|Zq| > 1.2$  and  $P < 0.05$ ) comparing p110α<sup>nKO</sup> versus control (left), p110β<sup>nKO</sup> versus control (center), and p110β<sup>nKO</sup> versus p110α<sup>nKO</sup> (right). Each point represents the average fold change of one protein and the  $P$  value for that comparison. Dashed lines represent significance thresholds [ $|Zq| > 1.2$  and  $-\log_{10}(P) > 1.3$ ]. Sign on the  $x$  axis represents up- or down-regulation. Names and outlined points represent top differentially up- or down-regulated proteins.



suggest that the p110α isoform plays a major role in maintaining proper brain growth and size, particularly as compared to p110β.

Previous studies have suggested that the PI3K pathway is important for both dendritic arborization and synaptogenesis (23, 26). Therefore, we hypothesized that the reductions we observed in hippocampal volume could be due to neuronal atrophy. To explore this

possibility, p110α<sup>nKO</sup> and p110β<sup>nKO</sup> mice were infected for 24 hours with a green fluorescent protein (GFP) Sindbis virus to reveal CA1 neuronal morphology (Fig. 2, F and G). As shown in Fig. 2 (H and I), p110α removal caused a marked decrease in dendritic complexity (as determined by Sholl analysis) and in the total length of both basal and apical dendrites when compared to control mice. A

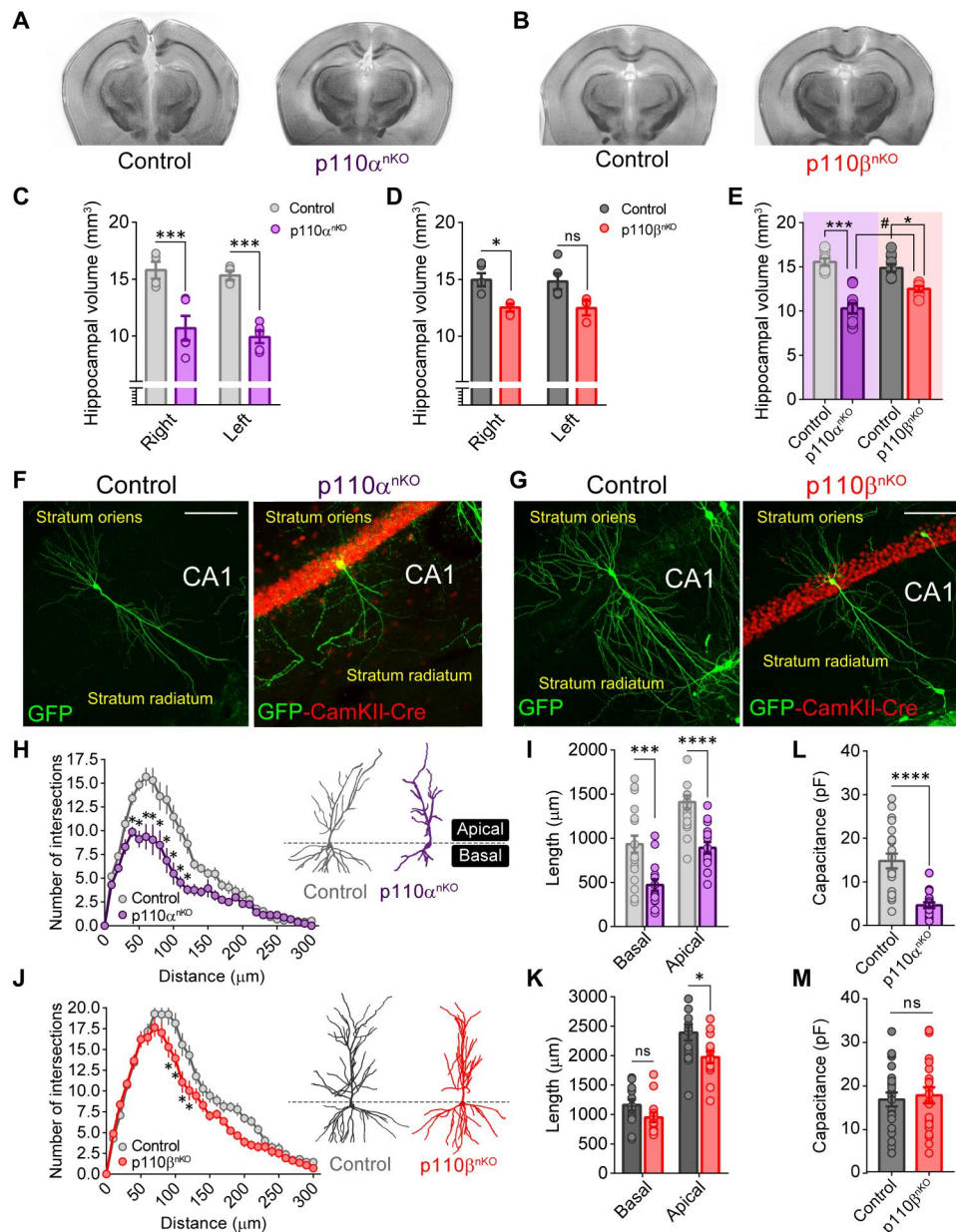


**Fig. 2. Differential contribution of p110 $\alpha$  and p110 $\beta$  to hippocampal size and neuronal morphology.** (A and B) Representative coronal sections of ex vivo magnetic resonance imaging from the brain of p110 $\alpha$ <sup>nKO</sup> and p110 $\beta$ <sup>nKO</sup> mice after AAV-CaMKII-Cre hippocampal infection. (C and D) Hippocampal volume quantification for the right and the left hemisphere in p110 $\alpha$ <sup>nKO</sup> and p110 $\beta$ <sup>nKO</sup> mice and their respective controls. Statistical significance was calculated by two-way repeated-measures analysis of variance (ANOVA) [(C)  $F(1,7) = 30.24, P = 0.0009$ ; (D)  $F(1,6) = 8.205, P = 0.03$ ] with Bonferroni's posttest (\*\*\*\* $P < 0.005$  and \* $P < 0.05$ ). ns, not significant. (E) Comparison between the hippocampal volume (right and left hemispheres for each mouse are displayed together) of p110 $\alpha$ <sup>nKO</sup> and p110 $\beta$ <sup>nKO</sup> mice. Statistical significance was calculated by two-way ANOVA [ $F(1,30) = 8.449, P = 0.007$ ] with Tukey's posttest (\*\*\*\* $P < 0.005$ , \* $P < 0.05$ , and # $P < 0.05$ ). p110 $\alpha$ <sup>flox/flox</sup>; vehicle,  $n = 4$ ; p110 $\alpha$ <sup>nKO</sup>,  $n = 5$ . p110 $\beta$ <sup>flox/flox</sup>; vehicle,  $n = 5$ ; p110 $\beta$ <sup>nKO</sup>,  $n = 3$ . (F and G) Merged representative images of CA1 green fluorescent protein (GFP)-expressing neurons from p110 $\alpha$ <sup>flox/flox</sup> and p110 $\beta$ <sup>flox/flox</sup> mice for all conditions (saline and AAV injected). After AAV infection, mice were superinfected with a Sindbis GFP virus. Scale bars, 100  $\mu$ m. (H and J) Sholl analysis depicting the mean number of intersections along the dendritic tree for uninfected (control) and AAV-infected CA1 pyramidal neurons from p110 $\alpha$ <sup>nKO</sup> and p110 $\beta$ <sup>nKO</sup> mice. Representative images of neurons traced for each condition are also shown. Statistical significance was calculated by two-way repeated-measures ANOVA [p110 $\alpha$ <sup>nKO</sup>:  $F(30,990) = 6.598, P < 0.0001$ ; p110 $\beta$ <sup>nKO</sup>:  $F(30,780) = 2.534, P < 0.0001$ ] with Bonferroni's posttest (\* $P < 0.05$ ). (I and K) Quantification of the total dendritic length for apical and basal dendrites for p110 $\alpha$ <sup>nKO</sup> and p110 $\beta$ <sup>nKO</sup> mice.  $n = 14$  to 20 neurons from at least three mice per condition. (L and M) Whole-cell membrane capacitance of AAV-infected (p110 $\alpha$ <sup>nKO</sup> and p110 $\beta$ <sup>nKO</sup>) and uninfected (control) CA1 pyramidal neurons from acute hippocampal slices. Data were compared by Mann-Whitney test (\* $P < 0.05$ , \*\*\*\* $P < 0.005$ , and \*\*\*\*\* $P < 0.0001$ ). p110 $\alpha$ <sup>flox/flox</sup>; vehicle,  $n = 21$ ; p110 $\alpha$ <sup>nKO</sup>,  $n = 18$  neurons. p110 $\beta$ <sup>flox/flox</sup>; vehicle,  $n = 23$ ; p110 $\beta$ <sup>nKO</sup>,  $n = 22$  neurons, from four mice per condition. Data are displayed as means  $\pm$  SEM.

Downloaded from https://www.science.org at Centro Nacional de Investigaciones Cardiovasculares on November 24, 2022

slight decrease in dendritic branching was also found upon p110 $\beta$  deletion in apical dendrites (Fig. 2, J and K), although it was much less pronounced than in p110 $\alpha$ -deleted neurons. As a complementary approach, we measured whole-cell membrane capacitance from patch-clamp electrophysiological recordings in acute hippocampal slices as an indicator of total cell surface (Fig. 2, L and M). In agreement with our morphological analysis, whole-cell membrane capacitance was strongly reduced in neurons from p110 $\alpha$ <sup>nKO</sup> mice but showed no differences in p110 $\beta$ <sup>nKO</sup> neurons when compared to controls. Therefore, these combined results reinforce the notion that p110 $\alpha$  activity is specifically required for the maintenance of proper dendritic and neuronal architecture.

We then analyzed spine density and morphology from GFP-expressing neurons in p110 $\alpha$ <sup>nKO</sup> and p110 $\beta$ <sup>nKO</sup> mice. p110 $\alpha$  deletion also promoted a marked reduction in spine density, which remained unaltered in the absence of p110 $\beta$  (Fig. 3, A and B). Remaining spines from p110 $\alpha$ <sup>nKO</sup> mice were wider and had larger head area as compared to control mice (Fig. 3, C, D, and G; and fig. S6, A and B), without changes in spine length (fig. S6C). In contrast, the absence of p110 $\beta$  had a very minor (although statistically significant) reduction of the spine head area (Fig. 3, E, F, and H) without changes in spine width or length (fig. S6, D to F). Next, we evaluated synaptic structure in more detail in the CA1 region of the hippocampus (stratum radiatum) by performing electron microscopy imaging of synapses in p110 $\alpha$ <sup>nKO</sup> and p110 $\beta$ <sup>nKO</sup>. As shown in Fig. 3 (I to L), compared to controls, spines from p110 $\alpha$ <sup>nKO</sup> neurons had longer and thicker postsynaptic densities. In contrast, the length and thickness of postsynaptic densities from p110 $\beta$ <sup>nKO</sup> mice were not altered, as compared to controls (fig. S7).

Together, these results evidence that absence of p110 $\alpha$  leads to a marked remodeling of neuronal and synaptic morphology, with a major retraction of dendritic arborization and loss of spines, which is accompanied by an enlargement of remaining postsynaptic structures. These changes are much more modest in p110 $\beta$ <sup>nKO</sup> neurons, indicating that PI3K-dependent regulation of neuronal morphology and postsynaptic structure is mainly mediated by the p110 $\alpha$  isoform.

### Absence of p110 $\alpha$ and p110 $\beta$ causes an accumulation of vesicles at the presynaptic terminals

The electron microscopy analysis presented above also allowed us to investigate potential alterations at presynaptic terminals in neurons lacking p110 $\alpha$  or p110 $\beta$ . As shown in Fig. 4 (A to F), both p110 $\alpha$ <sup>nKO</sup> and p110 $\beta$ <sup>nKO</sup> neurons showed a marked increase (about threefold) in the number of synaptic vesicles per synapse, as compared to neurons from control mice. These vesicles spread throughout larger distances from the synaptic cleft, as shown in the cumulative distributions in Fig. 4G. To get further insight into the potential functional relevance of this vesicle accumulation, we then quantified synaptic vesicle density in close proximity (100 nm) to the synaptic membrane as a morphological approximation to the pool of readily releasable vesicles (41). In this case, we observed a statistically significant increase (about twofold) in vesicle density for p110 $\beta$ <sup>nKO</sup> neurons, while there were no differences in p110 $\alpha$ <sup>nKO</sup> neurons, as compared to their controls (Fig. 4H). The difference in synaptic vesicle density in this region was also statistically different between p110 $\alpha$ <sup>nKO</sup> and p110 $\beta$ <sup>nKO</sup> conditions. To note, these measurements are expressed as vesicle density, therefore normalizing for differences in the length of the synaptic membrane. On the

other hand, the diameter of the presynaptic vesicles was not altered in p110 $\alpha$ <sup>nKO</sup> or p110 $\beta$ <sup>nKO</sup> neurons (Fig. 4, I to J). Overall, these analyses support a more prominent role at the presynaptic terminal for p110 $\beta$ , as compared to p110 $\alpha$ .

### p110 $\alpha$ and p110 $\beta$ control basal synaptic transmission in opposite directions

Our morphological data indicate that p110 $\alpha$  and p110 $\beta$  are differentially required for maintaining proper neuronal morphology at both postsynaptic and presynaptic level. To evaluate the functional impact of these morphological observations, we first evaluated basal synaptic transmission by extracellular recordings of Schaffer collateral-CA1 synapses from acute hippocampal slices of p110 $\alpha$ <sup>nKO</sup> and p110 $\beta$ <sup>nKO</sup> mice (see Fig. 5A for experimental configuration). Field excitatory postsynaptic potentials (fEPSPs) were measured in response to increasing stimulus intensities to generate input/output curves. We found that the genetic deletion of p110 $\alpha$  and p110 $\beta$  caused opposite effects on basal synaptic transmission. Thus, slices from p110 $\alpha$ <sup>nKO</sup> mice displayed a decrease in synaptic responses (Fig. 5B), whereas the absence of p110 $\beta$  produced an enhancement of synaptic transmission (Fig. 5C). None of these manipulations altered the excitability of the Schaffer collateral axons, as determined by presynaptic fiber volley amplitude (fig. S8, A and B). We did not find any differences in the ratio of AMPAR to NMDAR responses in whole-cell voltage-clamp recordings of CA1 neurons from p110 $\alpha$  and p110 $\beta$  mice (Fig. 5, D and E), suggesting that AMPAR- and NMDAR-mediated synaptic transmissions were altered to the same extent in p110 $\alpha$ <sup>nKO</sup> and p110 $\beta$ <sup>nKO</sup> CA1 neurons. Next, as a measurement of presynaptic function, we evaluated the paired-pulse ratio (PPR) of fEPSPs in hippocampal CA1 pyramidal neurons in response to two consecutive stimulations (50 ms apart). When p110 $\alpha$  was removed, PPR remained similar to control slices (Fig. 5F), while PPR was significantly reduced in p110 $\beta$ <sup>nKO</sup> slices (Fig. 5G). These results suggest that the absence of p110 $\beta$  produces an increased probability of glutamate release. These results are in good agreement with the enhanced synaptic transmission in p110 $\beta$ -lacking slices (Fig. 5C) and may also fit with the accumulation of neurotransmitter vesicles in close proximity to the presynaptic membrane, as observed in our morphological analysis (Fig. 4H). Incidentally, the decreased basal transmission in p110 $\alpha$ -lacking slices is also consistent with the marked reduction in spine density in these animals (Fig. 3A). Overall, this initial electrophysiological characterization reinforces the notion of a prevalent role of the p110 $\beta$  isoform in presynaptic mechanisms, while the p110 $\alpha$  isoform would exert its actions on neuronal architecture and postsynaptic structure.

### p110 $\alpha$ and p110 $\beta$ control different forms of synaptic plasticity

We next examined the contribution of p110 $\alpha$  and p110 $\beta$  to two forms of synaptic plasticity that have been shown to require PI3K activity, namely, NMDAR-dependent LTP and mGluR-dependent LTD (12–18, 42). LTP was induced by theta-burst stimulation (TBS) and mGluR-LTD by paired-pulse low-frequency stimulation in the presence of D,L-2-amino-5-phosphonovaleric acid (APV; NMDAR antagonist), in acute hippocampal slices from p110 $\alpha$ <sup>nKO</sup> and p110 $\beta$ <sup>nKO</sup> mice. We found that the absence of both p110 $\alpha$  and p110 $\beta$  significantly impaired LTP expression when compared to their respective control mice (Fig. 6, A and B). In contrast,

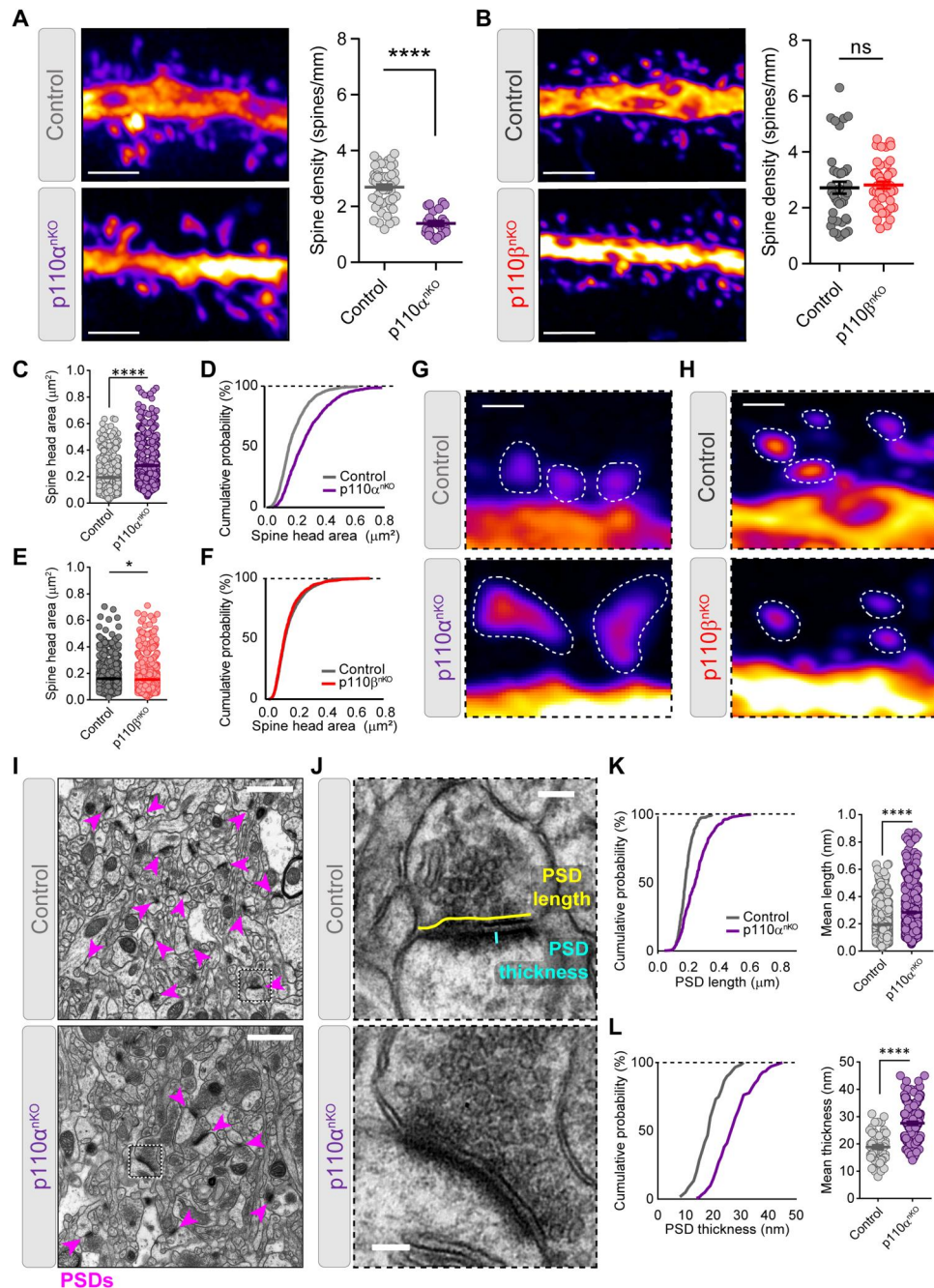


**Fig. 3. p110 $\alpha$  is required to maintain synaptic density and postsynaptic morphology in CA1 neurons.** (A and B) Quantification of spine density from CA1 neuron dendrites from p110 $\alpha$ <sup>nKO</sup> (A) and p110 $\beta$ <sup>nKO</sup> (B) and their respective saline control mice. Representative confocal images of GFP dendrites are shown in the left side of each graph. Scale bars, 2  $\mu$ m. Statistical differences between conditions were assessed by Mann-Whitney test: (A) \*\*\*\* $P$  < 0.0001 versus control and (B)  $P$  = 0.314 versus control. p110 $\alpha$ <sup>flx/flx</sup>; vehicle,  $n$  = 54; p110 $\alpha$ <sup>nKO</sup>,  $n$  = 24 dendrites. p110 $\beta$ <sup>flx/flx</sup>; vehicle,  $n$  = 40; p110 $\beta$ <sup>nKO</sup>,  $n$  = 47 dendrites, from five mice per condition. (C to F) Quantification of mean spine head area and cumulative distributions from neurons of p110 $\alpha$ <sup>nKO</sup> (C and D) and p110 $\beta$ <sup>nKO</sup> (E and F) mice. Data were analyzed by Mann-Whitney test: (C) \*\*\*\* $P$  < 0.0001 versus control and (E) \* $P$  < 0.05 versus control. p110 $\alpha$ <sup>flx/flx</sup>; vehicle,  $n$  = 1422; p110 $\alpha$ <sup>nKO</sup>,  $n$  = 792 spines. p110 $\beta$ <sup>flx/flx</sup>; vehicle,  $n$  = 1503; p110 $\beta$ <sup>nKO</sup>,  $n$  = 1457 spines, from three mice per condition. (G and H) Representative spines for the quantifications shown in (C) to (F). Scale bars, 0.5  $\mu$ m. (I and J) Representative electron micrograph examples from CA1 stratum radiatum of control and p110 $\alpha$ <sup>nKO</sup> mice. Higher-magnification pictures from representative synapses are shown in (J), with drawings indicating calculation of postsynaptic density (PSD) length and thickness. Arrowheads in pink indicate examples of PSDs. Scale bars, 1  $\mu$ m (I) and 0.2  $\mu$ m (J). (K and L) Cumulative frequency distributions (left) and scatter dot plots (right) for PSD length (K) and PSD thickness (L) in control and p110 $\alpha$ <sup>nKO</sup> synapses. Data were compared by Mann-Whitney test (\*\*\*\* $P$  < 0.0001 versus control). Number of synapses on each experiment (control and p110 $\alpha$ <sup>nKO</sup>, three mice per condition):  $n$  = 250 and 336 (PSD length) and  $n$  = 60 and 144 (PSD thickness). Data are shown as means + SEM.

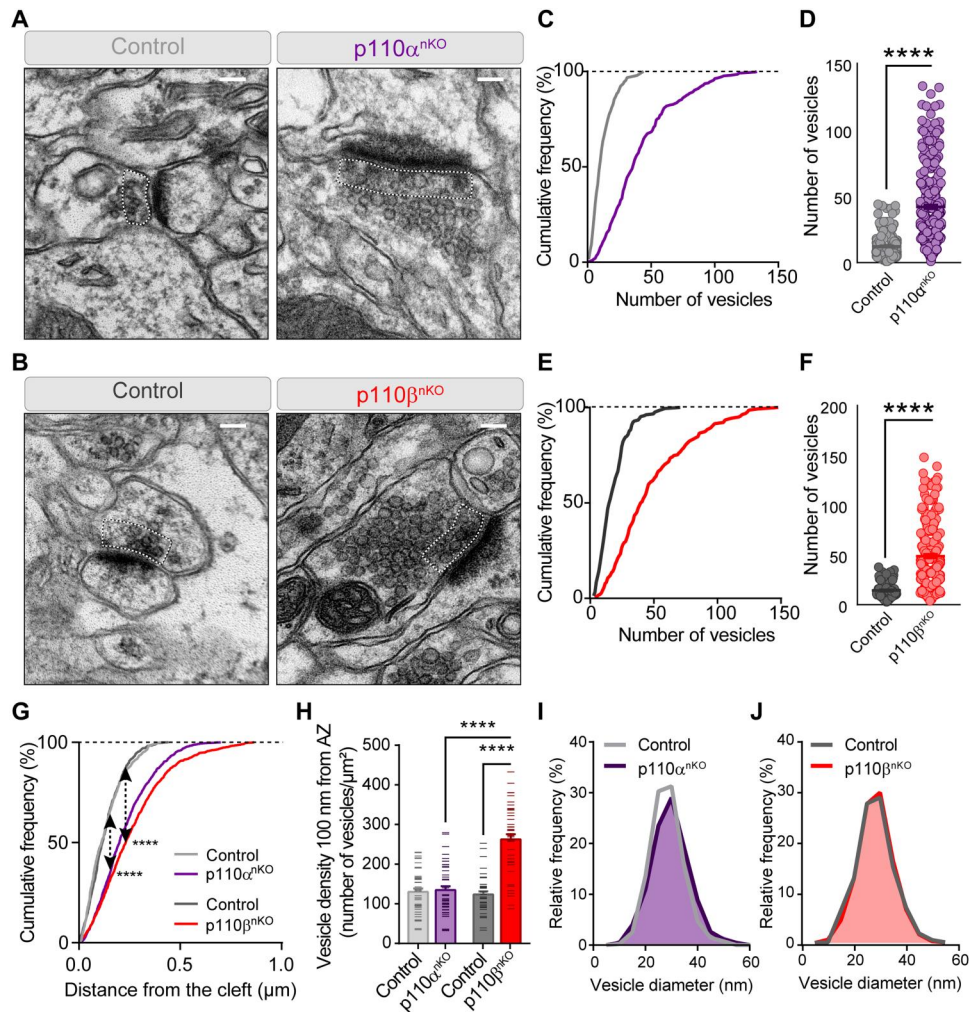


**Fig. 4. Lack of p110 $\alpha$  or p110 $\beta$  results in an accumulation of presynaptic vesicles.** (A and B) Representative electron micrograph examples from CA1 stratum radiatum of p110 $\alpha$ <sup>nKO</sup> (A) and p110 $\beta$ <sup>nKO</sup> (B) and their respective controls. Dotted lines depict the area within 100 nm of the synaptic cleft that was used for quantification in (H). Scale bars, 0.1  $\mu$ m. (C to F) Cumulative distributions and scatter plots for the number of vesicles per presynaptic terminal in p110 $\alpha$ <sup>nKO</sup> (C and D) and p110 $\beta$ <sup>nKO</sup> (E and F). \*\*\*\* $P$  < 0.0001 versus control mice from Mann-Whitney test. Number of synapses: control,  $n$  = 249; p110 $\alpha$ <sup>nKO</sup>,  $n$  = 347; control,  $n$  = 213; p110 $\beta$ <sup>nKO</sup>,  $n$  = 283. (G) Cumulative frequency distribution of the vesicle distance to the synaptic cleft. \*\*\*\* $P$  < 0.0001 from Kolmogorov-Smirnov test (arrows depict Kolmogorov-Smirnov statistic). Number of synaptic vesicles: 466 (control p110 $\alpha$ , from 40 presynaptic terminals), 1302 (p110 $\alpha$ <sup>nKO</sup>, from 30 presynaptic terminals), 690 (control p110 $\beta$ , from 40 presynaptic terminals), and 1080 (p110 $\beta$ <sup>nKO</sup>, from 20 presynaptic terminals). (H) Bar plots for the vesicle density within 100 nm from the synaptic cleft. \*\*\*\* $P$  < 0.0001 versus control from Mann-Whitney test. Number of synapses on each experiment (two mice per condition):  $n$  = 45 and 42 (control p110 $\alpha$  and p110 $\alpha$ <sup>nKO</sup>) and  $n$  = 44 and 37 (control p110 $\beta$  and p110 $\beta$ <sup>nKO</sup>). (I and J) Frequency histograms of synaptic vesicle size from p110 $\alpha$  (I) (purple area) and p110 $\beta$  (J) (red area) knockout neurons and their respective controls (gray lines). Vesicle size was measured from electron microscopy pictures where the active zone membrane was clearly visible. p110 $\alpha$ <sup>flox/flox</sup>: vehicle,  $n$  = 99; p110 $\alpha$ <sup>nKO</sup>:  $n$  = 134 synapses. p110 $\beta$ <sup>flox/flox</sup>: vehicle  $n$  = 50; p110 $\beta$ <sup>nKO</sup>:  $n$  = 109 synapses. Three mice per condition for the AAV infections and one or two mice for the vehicle.

mGluR-LTD was selectively abolished in slices from p110 $\beta$ <sup>nKO</sup> mice (Fig. 6, C and D), indicating the specific requirement of the p110 $\beta$  isoform for mGluR-LTD. In addition, neither p110 $\alpha$  nor p110 $\beta$  were required for NMDAR-dependent LTD (fig. S8, C and D), in agreement with previous studies (20).

To bypass potential effects of the semichronic genetic deletion of p110 $\alpha$  or p110 $\beta$ , we used the isoform-specific inhibitors A66 and TGX221 (43, 44) to pharmacologically suppress the catalytic activity from the p110 $\alpha$  and p110 $\beta$  isoforms, respectively, in a more acute manner (Fig. 7) (to note, bath application of PI3K inhibitors is not restricted to neurons, as it is the case with the p110 $\alpha$ <sup>nKO</sup> or p110 $\beta$ <sup>nKO</sup> mice). We chose the concentrations of 2.5  $\mu$ M for A66

and 0.5  $\mu$ M for TGX221 based on their effect on PI3K pathway activation, as reported by phosphorylation of Akt (pAkt) at Thr<sup>308</sup> (Fig. 7, A and B). Similar to our previous results with acute slices from p110 $\alpha$ <sup>nKO</sup> and p110 $\beta$ <sup>nKO</sup> mice, we did not find any differences in AMPAR/NMDAR ratios from A66-, TGX221-, and vehicle-treated slices (Fig. 7C). NMDAR-dependent LTP was evaluated under whole-cell voltage-clamp configuration by pairing presynaptic stimulation of Schaffer collaterals (3 Hz) with postsynaptic depolarization (0 mV) of CA1 neurons (45–47). Under this configuration, LTP was abolished in A66-treated slices. On the other hand, TGX221 appeared to reduce the extent of synaptic potentiation, although the effect was not statistically significant (Fig. 7,

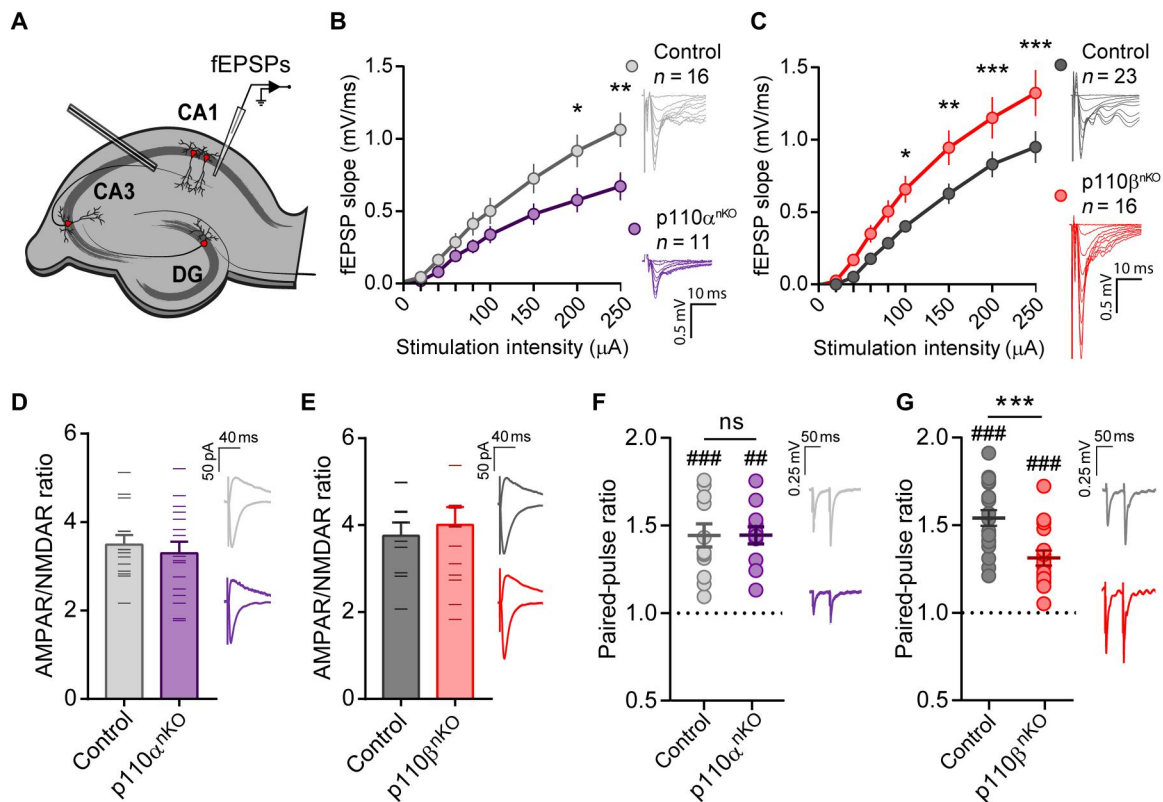


**Fig. 5. Neuronal p110 $\alpha$  and p110 $\beta$  isoforms have different effects on basal transmission.** (A) Experimental configuration for extracellular field recordings in acute slices. DG, dentate gyrus. (B and C) Input-output curves of the extracellular fEPSPs from p110 $\alpha$ <sup>nKO</sup> (B) and p110 $\beta$ <sup>nKO</sup> (C) slices evoked at different stimulation intensities. p110 $\alpha$ <sup>nKO</sup>:  $n = 16$  slices from five mice; two-way repeated-measures ANOVA,  $F(8,200) = 4.177$ ,  $P = 0.0001$ . p110 $\beta$ <sup>nKO</sup>:  $n = 18$  to 16 slices from five mice; two-way repeated-measures ANOVA,  $F(8,256) = 5.97$ ,  $P < 0.0001$ . Bonferroni's posttest (\* $P < 0.05$ , \*\* $P < 0.01$ , \*\*\* $P < 0.005$ ). Representative traces from one experiment for each condition are depicted on the right. Scale bar, 0.5 mV, 10 ms. (D and E) Bar graph of the ratio of AMPAR- to NMDAR-mediated excitatory postsynaptic currents (EPSCs) in CA1 pyramidal neurons from p110 $\alpha$ <sup>nKO</sup> and p110 $\beta$ <sup>nKO</sup> mice recorded on whole-cell voltage clamp configuration. AMPAR responses were measured at  $-60$  mV and NMDAR responses at  $+40$  mV, 60 ms after stimulation of the Schaffer collaterals. p110 $\alpha$ <sup>flox/flox</sup>: control,  $n = 14$ ; p110 $\alpha$ <sup>nKO</sup>,  $n = 16$  cells. p110 $\beta$ <sup>flox/flox</sup>: control,  $n = 10$ ; p110 $\beta$ <sup>nKO</sup>,  $n = 14$  cells from three mice per condition. Representative traces are shown on the right of each graph. Scale bars, 50 pA, 40 ms. No statistically significant differences were observed by two-tailed nonparametric Mann-Whitney test. (F and G) Average values of PPRs from fEPSP recordings from p110 $\alpha$ <sup>nKO</sup> (F) and p110 $\beta$ <sup>nKO</sup> (G) slices with 50-ms interstimulus interval. Individual values for each condition are displayed as a dot plot. p110 $\alpha$ <sup>flox/flox</sup>: vehicle,  $n = 13$ ; p110 $\alpha$ <sup>nKO</sup>,  $n = 12$  slices. p110 $\beta$ <sup>flox/flox</sup>: vehicle,  $n = 19$ ; p110 $\beta$ <sup>nKO</sup>,  $n = 16$  slices from more than four mice per condition. Representative traces for each condition are shown on the right of each panel. Statistical differences between conditions were assessed with Mann-Whitney test (\*\*\* $P < 0.001$ ). Wilcoxon matched-pairs signed-rank test was used to assess significant paired-pulse facilitation (## $P < 0.01$  and ### $P < 0.005$ ).

D and E). mGluR LTD was also carried out under whole-cell voltage-clamp configuration with low-frequency paired pulses of Schaffer collaterals. In this case, the p110 $\beta$  inhibitor (TGX221) completely abolished mGluR-LTD expression, whereas the p110 $\alpha$  inhibitor (A66) did not have any effect (Fig. 7, F and G). Therefore, these results with pharmacological inhibition of p110 $\alpha$  and p110 $\beta$  isoforms essentially reproduce those obtained with p110 $\alpha$ <sup>nKO</sup> and p110 $\beta$ <sup>nKO</sup> mice, supporting the interpretation of a selective requirement of p110 $\beta$  for mGluR LTD and pointing to a joint contribution of p110 $\alpha$  and p110 $\beta$  to LTP (perhaps with a preferential role of p110 $\alpha$ ).

#### Presynaptic or postsynaptic loci of action for p110 $\alpha$ and p110 $\beta$ during synaptic plasticity

The combination of our proteomic and morphological data, together with the specific effect of p110 $\beta$  in paired-pulse facilitation, suggests that p110 $\alpha$  and p110 $\beta$  could be exerting their synaptic functions differentially at the pre- or postsynaptic compartments.

To further explore this possibility, we restricted the AAV-CaMKII-Cre injections on p110 $\alpha$  and p110 $\beta$  floxed mice to the CA1 hippocampal region (Fig. 8, A and B). This strategy allowed us to specifically remove p110 $\alpha$  or p110 $\beta$  from postsynaptic CA1 neurons and explore whether specific changes in basal transmission and synaptic plasticity are still present. Deletion of p110 $\alpha$  in CA1 postsynaptic neurons significantly reduced basal transmission (Fig. 8C), blocked NMDAR-dependent LTP (Fig. 8E), and did not alter PPR (Fig. 8D) or fiber volley amplitude (Fig. 8E), similar to the results obtained with whole hippocampal infection (Figs. 5 and 6). These results strongly suggest that the synaptic locus of action of p110 $\alpha$  is confined within the postsynaptic compartment.

On the other hand, p110 $\beta$ -specific deletion from postsynaptic CA1 neurons no longer altered basal synaptic transmission (Fig. 8F) or PPR (Fig. 8G), in contrast with the results obtained with the full p110 $\beta$ <sup>nKO</sup> (Fig. 5, C and G). These results suggest that these parameters are controlled by p110 $\beta$  at the presynaptic compartment. To note, fiber volley amplitude was not affected by



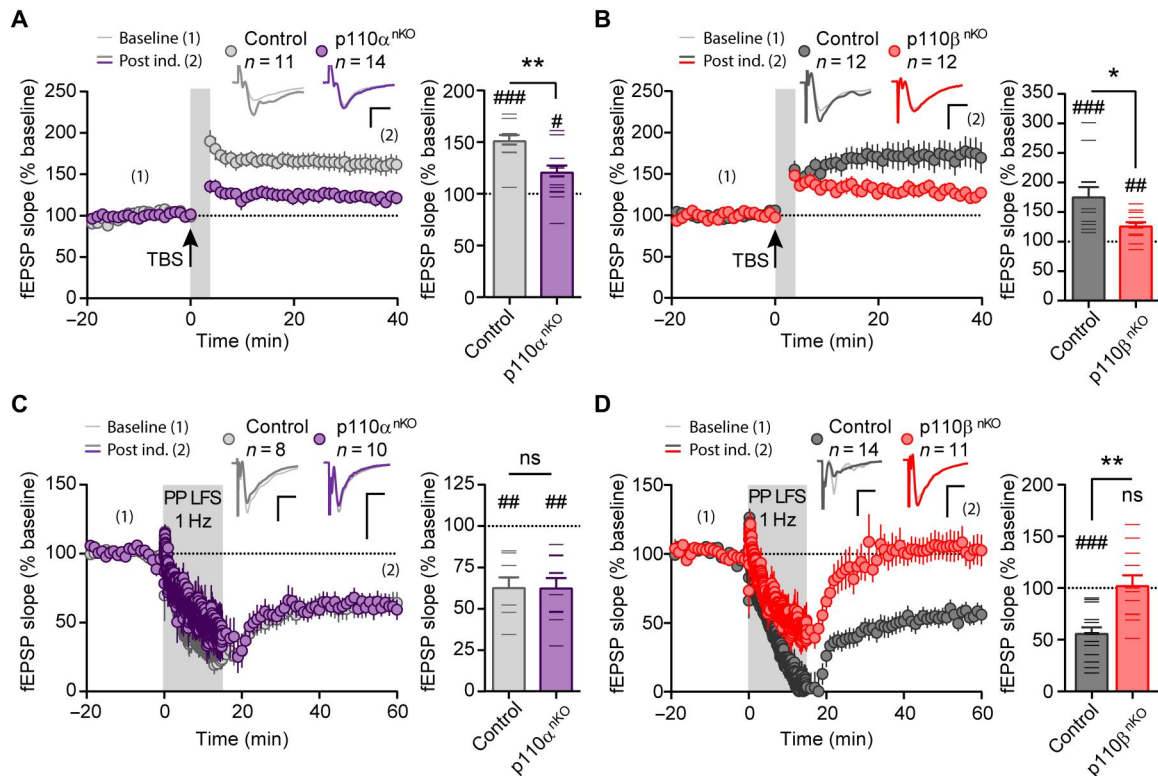


**Fig. 6. Neuronal p110 $\alpha$  and p110 $\beta$  isoforms are differentially required for synaptic plasticity.** (A and B) Time course of NMDAR-dependent LTP induced by TBS in p110 $\alpha$ <sup>nKO</sup> (A) and p110 $\beta$ <sup>nKO</sup> (B) slices and their respective control mice. Wilcoxon statistical test was used to evaluate LTP expression with respect to baseline ( $\#P < 0.05$ ;  $\#\#P < 0.01$ ;  $\#\#\#P < 0.005$ ). Right: Bar graphs showing the average change in fEPSP slope from the last 5 min of the recording. Statistical differences between conditions were assessed with Mann-Whitney test ( $*P < 0.05$ ;  $**P < 0.01$ ). p110 $\alpha$ <sup>fllox/fllox</sup>; vehicle,  $n = 13$ ; p110 $\alpha$ <sup>nKO</sup>,  $n = 12$  slices. p110 $\beta$ <sup>fllox/fllox</sup>; vehicle,  $n = 19$ ; p110 $\beta$ <sup>nKO</sup>,  $n = 16$  slices from more than four mice per condition. Representative traces are shown above the graphs. (C and D) Time course of mGluR-dependent LTD induced by paired-pulse low-frequency stimulation (PP LFS) in the presence of APV in p110 $\alpha$ <sup>nKO</sup> (C) and p110 $\beta$ <sup>nKO</sup> slices (D) and their respective control mice. Right: Bar graphs showing the average fEPSP slope from the last 5 min of recording. Wilcoxon statistical test was used to evaluate LTD expression with respect to baseline ( $\#\#P < 0.01$ ;  $\#\#\#P < 0.005$ ). Statistical differences between conditions were assessed with Mann-Whitney test ( $**P < 0.01$ ). p110 $\alpha$ <sup>fllox/fllox</sup>; vehicle,  $n = 13$ ; p110 $\alpha$ <sup>nKO</sup>,  $n = 12$  slices. p110 $\beta$ <sup>fllox/fllox</sup>; vehicle,  $n = 19$ ; p110 $\beta$ <sup>nKO</sup>,  $n = 16$  slices from more than four mice per condition. Representative traces are shown above the graphs. For all panels, data are presented as means  $\pm$  SEM.

removal of p110 $\beta$  from postsynaptic CA1 neurons (fig. S8F), similar to the result obtained with the full p110 $\beta$ <sup>nKO</sup>. LTP was still impaired when p110 $\beta$  was removed specifically from CA1 neurons (Fig. 8H), suggesting that p110 $\beta$  is required at the postsynaptic compartment for its contribution to LTP. mGluR-LTD was completely preserved in postsynaptic p110 $\beta$  knockout neurons, as compared to control mice, both from extracellular fEPSP recordings (Fig. 8I) and from whole-cell recordings from individual CA1 knockout (infected) neurons (Fig. 8J). Together, these results point to a dual role of p110 $\beta$ : acting at the presynaptic terminal to control neurotransmitter release and to mediate mGluR-LTD while contributing to NMDAR-dependent LTP at the postsynaptic compartment.

### Neuronal deletion of p110 $\alpha$ or p110 $\beta$ in the adult hippocampus causes specific behavioral abnormalities

Given the specific contribution of p110 $\alpha$  and p110 $\beta$  isoforms to synaptic plasticity and neuronal architecture, we lastly evaluated whether deletion of neuronal p110 $\alpha$  and p110 $\beta$  has cognitive consequences in vivo. To this end, 4 weeks after hippocampal infection with AAV-CamKII-mCherry-Cre, p110 $\alpha$ <sup>nKO</sup>, p110 $\beta$ <sup>nKO</sup> mice, and their respective controls were tested for different behaviors, ranging from anxiety to memory and social behavior.

Spontaneous locomotor activity was evaluated in the open field test (see representative mouse trajectories in Fig. 9A). Both p110 $\alpha$ <sup>nKO</sup> and p110 $\beta$ <sup>nKO</sup> mice showed higher locomotor activity than control mice, which was reflected in longer distances traveled (Fig. 9, B and C), faster movement (fig. S9, A and B), and reduced immobility times (Fig. 9, D and E), as compared to control mice. The hyperlocomotion phenotype was qualitatively different between p110 $\alpha$ <sup>nKO</sup> and p110 $\beta$ <sup>nKO</sup> mice. Thus, p110 $\alpha$ <sup>nKO</sup> mice were hyperactive but showed habituation to the novel environment (reduction in locomotor activity over time) in the first few minutes (Fig. 9F). In contrast, p110 $\beta$ <sup>nKO</sup> mice continued being hyperactive for the whole duration of the test, suggesting a defective habituation when p110 $\beta$  was removed (Fig. 9G). The open field arena was also used to investigate basal anxiety levels (see definition of experimental zones in fig. S9C). We observed that the hyperlocomotion of both p110 $\alpha$ <sup>nKO</sup> and p110 $\beta$ <sup>nKO</sup> mice preferentially occurred at the periphery of the arena, where they traveled significantly longer distances (fig. S9, D and E) and spent longer time (fig. S9, F and G) than control mice. On the other hand, a more detailed analysis revealed an increase in exploratory activity for both p110 $\alpha$ <sup>nKO</sup> and p110 $\beta$ <sup>nKO</sup> mice in the borders of the arena, specifically rearing and olfactory investigation of the borders (fig. S9, H and I).

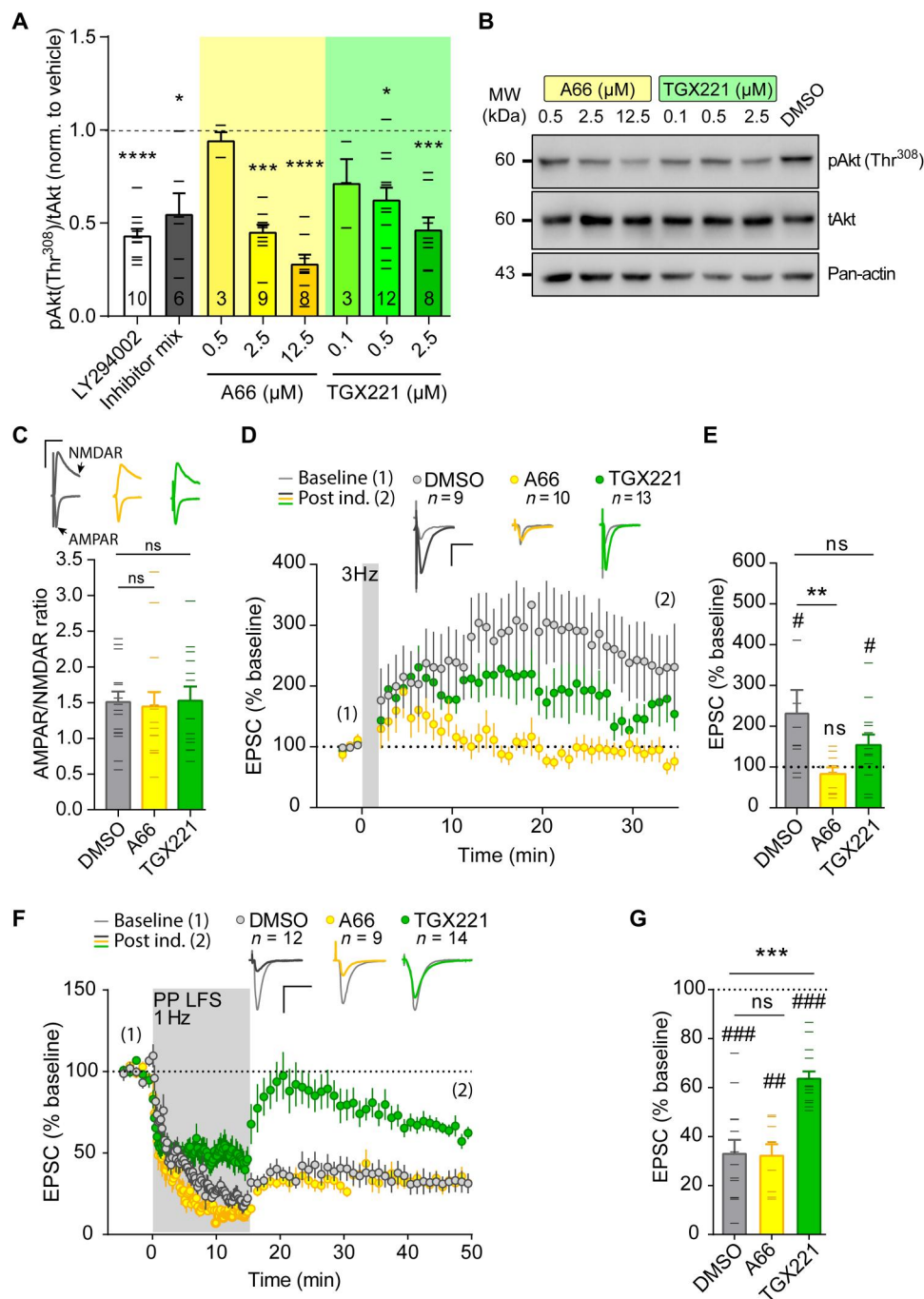
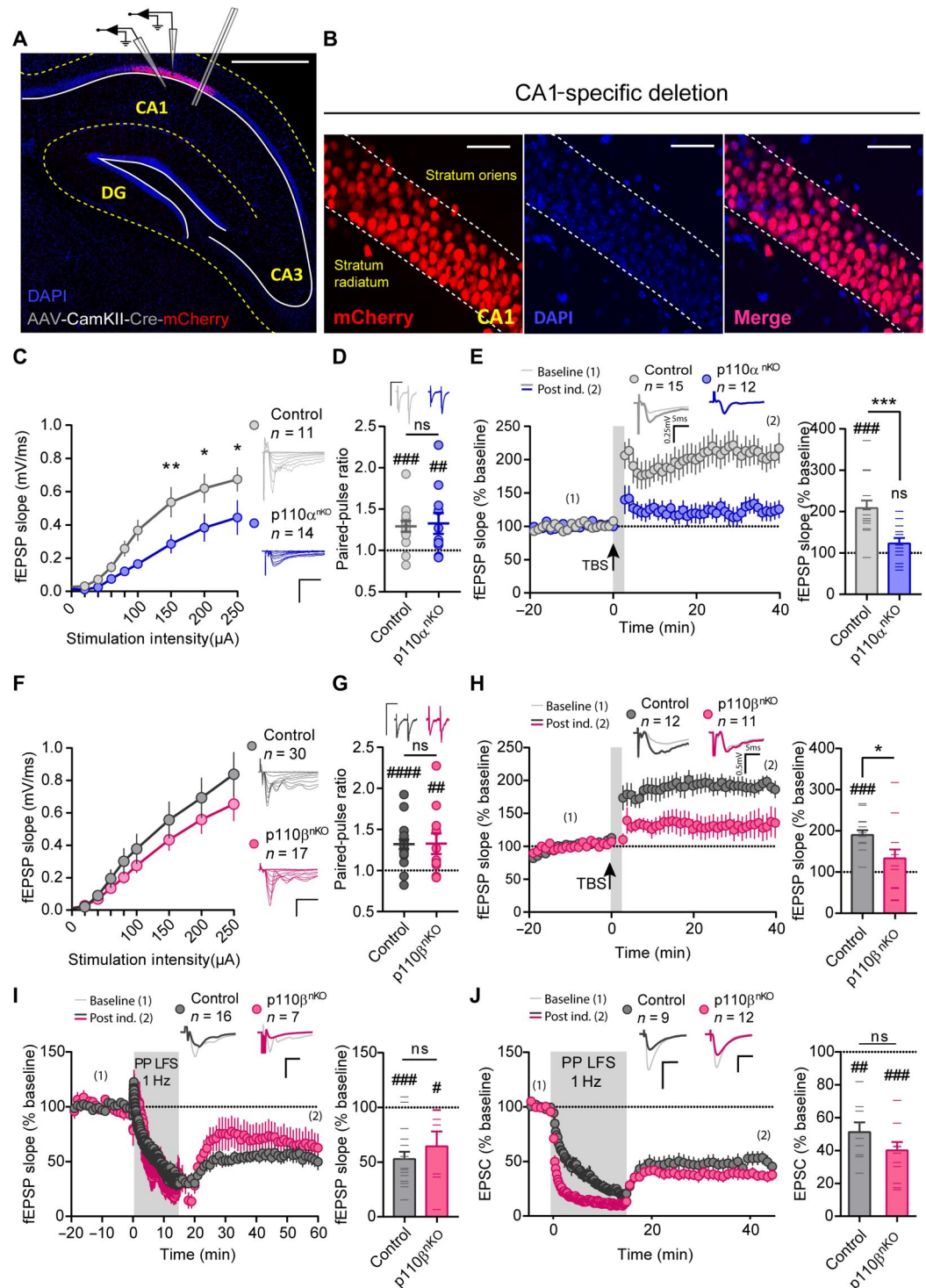


**Fig. 7. Effect of pharmacological inhibition of p110 $\alpha$  and p110 $\beta$  on basal transmission and synaptic plasticity.** (A) Quantification of the phospho/total ratio for Akt(Thr<sup>308</sup>) [pAkt(Thr<sup>308</sup>)/tAkt] from Western blots of whole extracts from organotypic slice cultures treated overnight with different concentrations of the p110 $\alpha$ -selective inhibitor (A66) or the p110 $\beta$ -selective inhibitor (TGX221), the nonselective PI3K inhibitor (10  $\mu$ M LY294002), or an inhibitor mix (0.5  $\mu$ M A66, 0.1  $\mu$ M TGX221, and 0.02  $\mu$ M CAL101-p110 $\delta$ -selective inhibitor). Statistical differences were assessed by Kruskal-Wallis nonparametric test and Dunn's multiple comparison test (\* $P$  < 0.05, \*\*\* $P$  < 0.001, and \*\*\*\* $P$  < 0.0001). (B) Representative images of Western blots. MW, molecular weight. (C) AMPAR/NMDAR ratios from slices treated as indicated.  $n$  = 15 [dimethyl sulfoxide (DMSO)], 14 (A66), 15 (TGX221) cells from  $n$  > 4 rats per condition. (D and F) Time course of normalized AMPAR-mediated EPSCs from baseline and after induction of NMDAR-dependent LTP (D) or mGluR-LTD (F). Representative traces before induction (1; thin lines) and for the last 5 min of the time course (2; thick lines) are depicted above the time course. Vertical gray shading indicates the induction protocol. (E and G) Summary bar plot of average EPSC amplitude for each cell from the last 5 min of recording. Wilcoxon matched-pairs signed-rank test (#) was used to assess statistically significant potentiation. Mann-Whitney test (\*) was used to evaluate significant differences between conditions. \*\* $P$  < 0.01, \*\*\* $P$  < 0.001, # $P$  < 0.05, ## $P$  < 0.01, and ### $P$  < 0.001. For all panels, data are presented as means  $\pm$  SEM.

**Fig. 8. Synaptic function and plasticity after postsynaptic removal of p110α or p110β.** (A and B) Representative images of CA1-infected hippocampus, as identified from mCherry fluorescence, and experimental configuration for extracellular fEPSP and whole-cell EPSC recordings. Scale bars, 500 μm (A) and 50 μm (B). (C and F) Input-output curves of fEPSP slopes versus stimulation intensity. (C) Control,  $n = 11$ ; p110α<sup>nKO</sup>,  $n = 14$  slices from four mice; two-way repeated-measures ANOVA,  $F(8,124) = 2.845$ ,  $P = 0.005$ . (F) Control,  $n = 30$ ; p110β<sup>nKO</sup>,  $n = 17$  slices from more than five mice; two-way repeated-measures ANOVA, ns. Bonferroni's posttest (\* $P < 0.05$  and \*\* $P < 0.01$ ).

Representative traces are depicted on the right of the plots. (D and G) Quantification of PPRs of fEPSPs. Representative traces are shown above the plots. (D) Control,  $n = 15$ ; p110α<sup>nKO</sup>,  $n = 11$ . (G) Control,  $n = 19$ ; p110β<sup>nKO</sup>,  $n = 11$  slices from more than five mice. (E, H, and I) Time course of normalized fEPSP responses from baseline and after induction of NMDAR-dependent LTP (E and H) or mGluR-dependent LTD (I), on p110α<sup>nKO</sup> (E) or p110β<sup>nKO</sup> (H and I) slices. Representative traces before induction (1; thin lines) and from the last 5 min of the time course (2; thick lines) are depicted above the time course. Right: Summary bar plot of fEPSP slope from the last 5 min of recording. (J) Similar to (I) but with whole-cell voltage-clamp recordings of EPSCs from individual CA1 neurons expressing Cre-mCherry. For all panels, statistical differences between conditions were assessed with Mann-Whitney test (\*). Wilcoxon matched-pairs signed-rank test (#) was used to assess statistically significant paired-pulse facilitation (D and G), potentiation (E and H), and depression (I and J). \* $P < 0.05$ , \*\*\* $P < 0.001$ , # $P < 0.05$ , ## $P < 0.01$ , ### $P < 0.005$ , #### $P < 0.001$ .  $n$ : number of slices (C to I) or number of individual cells (J). Bars represent means  $\pm$  SEM.



The increase in locomotion at the periphery of the open field could suggest an increased anxiety. Therefore, we next tested p110α<sup>nKO</sup> and p110β<sup>nKO</sup> mice in the elevated plus maze as a more direct assay to evaluate anxiety. However, using this test, we did not find any significant difference between control and p110α<sup>nKO</sup> or p110β<sup>nKO</sup> mice in traveled distance (fig. S10A), time spent (fig. S10B), or number of visits (fig. S10C) to open or closed arms.

Therefore, according to this assay and the increase in exploratory activity in the open field, deletion of p110α or p110β isoforms does not appear to produce anxiogenic effects.

We next evaluated working memory in p110α<sup>nKO</sup> or p110β<sup>nKO</sup> mice with the alternation test in the Y-maze. In this task, while exploring the maze, control mice typically alternated between the three arms and avoided repetitions of two arms (see schematic

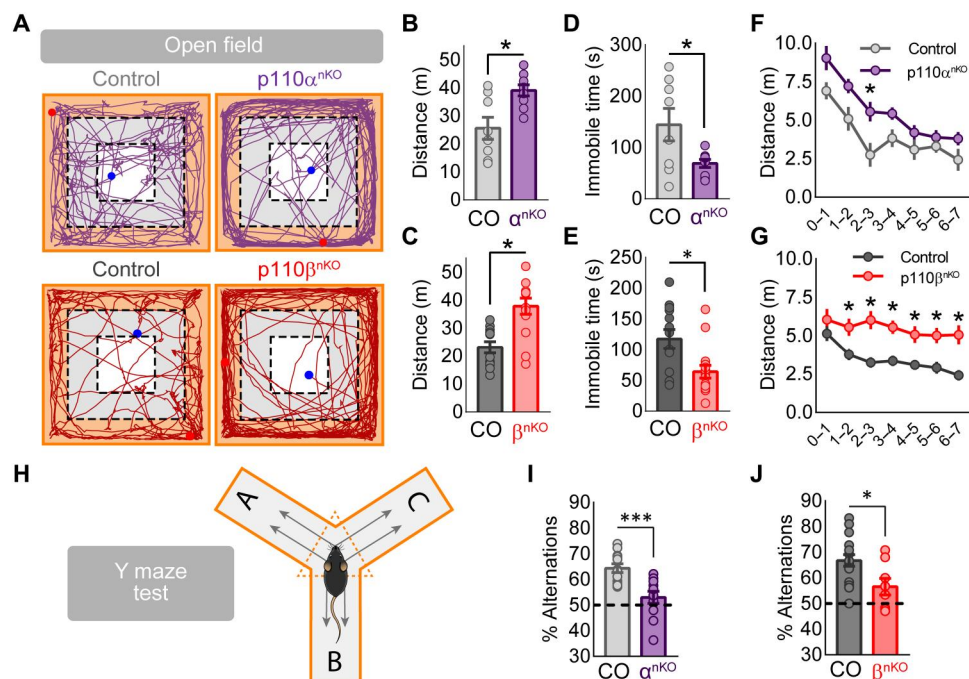


**Fig. 9. Open field and Y-maze tests on p110 $\alpha$ <sup>nKO</sup> and p110 $\beta$ <sup>nKO</sup> animals.** (A to G) Mice were tested in the open field for exploring locomotor behavior. Mice were placed individually in the center of an open field arena (40 cm by 40 cm by 40 cm) and allowed to habituate and freely explore the area for 7 min. (A) Representative paths of ambulation from p110 $\alpha$ <sup>nKO</sup> (top), p110 $\beta$ <sup>nKO</sup> (bottom), and their respective controls for the entire duration of the test. Periphery, inner, and center zones are also shown in orange, gray, and white, respectively. (B and C) Quantification of the total traveled distance for the entire duration of the test for p110 $\alpha$  (B) and p110 $\beta$  (C) floxed mice. (D and E) Quantification of the mean time that mice spend immobile in the arena for p110 $\alpha$  (D) and p110 $\beta$  (E) floxed mice. (F and G) Quantification of the mean traveled distance in time segments of 1 min for p110 $\alpha$  (F) and p110 $\beta$  (G) floxed mice. Mann-Whitney test was used to assess statistical differences between p110 $\alpha$ <sup>nKO</sup> or p110 $\beta$ <sup>nKO</sup> and controls (\* $P$  < 0.05). p110 $\alpha$ <sup>flx/flx</sup>: vehicle,  $n$  = 8; p110 $\alpha$ <sup>nKO</sup>,  $n$  = 9. p110 $\beta$ <sup>flx/flx</sup>: vehicle,  $n$  = 13; p110 $\beta$ <sup>nKO</sup>,  $n$  = 15. (H) Experimental scheme of the spontaneous alternation task that is performed on a Y-shaped maze. Mice are placed on the center region of the maze; the arm entrance order is recorded, and then the spontaneous alternation percentage is calculated. (I and J) Spontaneous alternation percentages from p110 $\alpha$ <sup>nKO</sup> (I) and p110 $\beta$ <sup>nKO</sup> (J) and their respective controls. Statistical analysis between conditions was performed with Mann-Whitney test (\*\*\* $P$  < 0.001 and \* $P$  < 0.05). p110 $\alpha$ <sup>flx/flx</sup>: control,  $n$  = 12; p110 $\alpha$ <sup>nKO</sup>,  $n$  = 12. p110 $\beta$ <sup>flx/flx</sup>: control,  $n$  = 16; p110 $\beta$ <sup>nKO</sup>,  $n$  = 8.

cartoon for the test in Fig. 9H). In contrast, both p110 $\alpha$ <sup>nKO</sup> and p110 $\beta$ <sup>nKO</sup> mice showed a marked reduction in the number of alternations, which may be indicative of impaired working memory or behavioral flexibility (Fig. 9, I and J) (48).

Next, we tested mice for spatial and episodic memory using the novel object location (NOL; fig. S11A) and novel object recognition (NOR; Fig. 10A) tests (NOLT and NORT, respectively). In the NOL task, both p110 $\alpha$ <sup>nKO</sup> and p110 $\beta$ <sup>nKO</sup> mice displayed normal spatial learning compared to control mice (fig. S11, B and C), as indicated from the preference to explore the object located in a new location. In contrast, in the NORT, we found that while control and p110 $\alpha$ <sup>nKO</sup> mice preferentially explored the novel object (Fig. 10B), p110 $\beta$ <sup>nKO</sup> mice failed to discriminate the novel versus the familiar object (Fig. 10C). This is reflected in the time exploring the new versus the familiar object and is quantified by the recognition index (Fig. 10, B and C). These results suggest that p110 $\beta$ , but not p110 $\alpha$ , is required for object recognition memory. In addition, both p110 $\alpha$ <sup>nKO</sup> and p110 $\beta$ <sup>nKO</sup> mice displayed normal habituation after object reexposure, as compared to their saline-injected controls (fig. S11, D to F).

Last, we evaluated whether the absence of p110 $\alpha$  or p110 $\beta$  alters social behavior. For that purpose, we used the three-chamber sociability and social novelty tests (see Fig. 10D for a schematic

representation of these assays) (49). In the sociability task, while control mice spent more time exploring a stranger mouse (S1) compared to an inanimate object (O), both p110 $\alpha$ <sup>nKO</sup> and p110 $\beta$ <sup>nKO</sup> spent similar times interacting with the mouse and the inanimate object; this was reflected in a reduction of the social preference index (Fig. 10, E and F). Next, in the social novelty test, control mice spent more time interacting with a stranger mouse (S2) than with the familiar one (S1). In contrast, both p110 $\alpha$ <sup>nKO</sup> and p110 $\beta$ <sup>nKO</sup> mice displayed a lack of preference for interaction with either mouse (Fig. 10, G and H), which was more evident (and statistically different from control) in the case of p110 $\beta$ <sup>nKO</sup>. Therefore, these results suggest that removal of p110 $\alpha$  or p110 $\beta$  impairs social behavior, both at the level of social preference and social memory.

## DISCUSSION

In this work, using a gene deletion approach in the hippocampus of adult mice, we have been able to ascribe specific functions to the major catalytic isoforms of type I PI3K, p110 $\alpha$ , and p110 $\beta$ , with respect to neuronal structure, synaptic plasticity, and cognitive performance. This information sheds light into how PI3K activity mediates apparently antagonistic functions, such as mGluR-dependent synaptic depression and NMDAR-dependent synaptic potentiation.

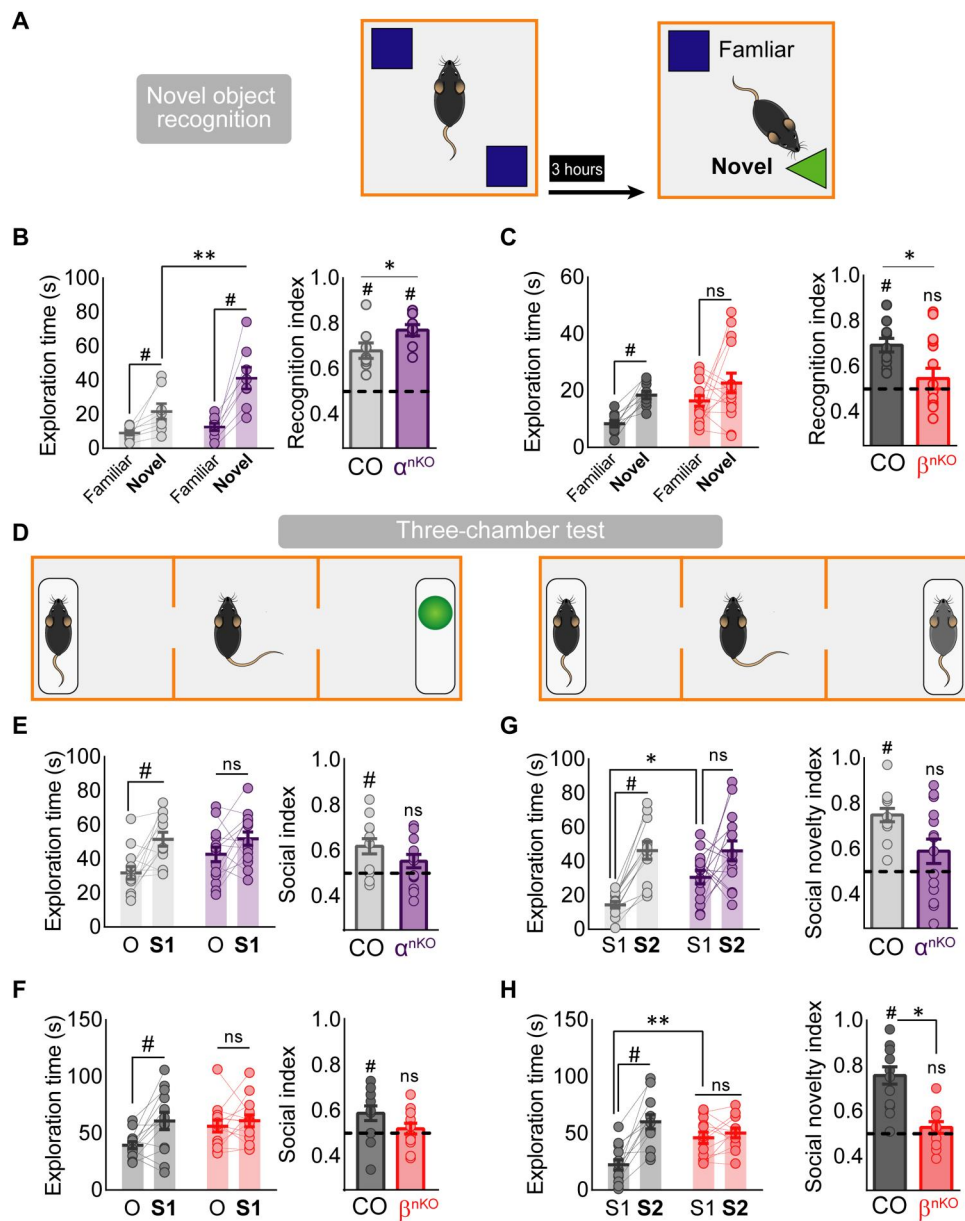


**Fig. 10. Novel object recognition and sociability tests on p110 $\alpha^{nKO}$  and p110 $\beta^{nKO}$  animals.** (A) Diagram of the NOR test. (B and C) Left graph: Exploration time of novel and familiar objects for p110 $\alpha$  (B) and p110 $\beta$  (C) floxed mice. Statistical significance according to two-way repeated-measures ANOVA [ $F(1,14) = 5.636, P = 0.036$ ; Bonferroni's posttest:  $**P < 0.01, *P < 0.05$ ]. Recognition index for p110 $\alpha$  (B) and p110 $\beta$  (C) floxed mice. Wilcoxon statistical test was used to assay discrimination ( $\#P < 0.05$ ), and data between groups was analyzed by two-tailed Mann-Whitney test ( $*P < 0.05$ ). p110 $\alpha^{flax/flax}$ : vehicle,  $n = 8$ ; p110 $\alpha^{nKO}$ ,  $n = 8$ . p110 $\beta^{flax/flax}$ : vehicle,  $n = 9$ ; p110 $\beta^{nKO}$ ,  $n = 13$ . (D) Schematic representation of the three-chamber social interaction task for the sociability (left) and for the social novelty (right) tests. (E and F) Exploration time for the subject (S1) versus the object (O), for p110 $\alpha^{nKO}$  [(E) left graph; two-way repeated-measures ANOVA,  $F(1,25) = 14.65, P = 0.0008$ ] and p110 $\beta^{nKO}$  (F) left graph; two-way repeated-measures ANOVA,  $F(1,25) = 7.836, P = 0.01$ ). Bonferroni's posttest,  $\#P < 0.05$ . Right graphs: Social index (percentage of time exploring the subject over the total exploration time) for p110 $\alpha^{nKO}$  (E) and p110 $\beta^{nKO}$  (F) mice. Wilcoxon statistical test was used to assay social preference ( $\#P < 0.05$ ). (G and H) Exploration time of a novel (S2) versus a familiar (S1) mouse for p110 $\alpha^{nKO}$  [(G) left graph; two-way repeated-measures ANOVA,  $F(1,24) = 23.87, P < 0.0001$ ] and p110 $\beta^{nKO}$  [(H) left graph; two-way repeated-measures ANOVA,  $F(1,23) = 31.11, P < 0.0001$ ] mice. Bonferroni's posttest:  $*P < 0.05; **P < 0.01$ . Right graphs: Social novelty index (percentage of time exploring the novel mouse over the total exploration time) for p110 $\alpha^{nKO}$  (G) and p110 $\beta^{nKO}$  (H) mice. Wilcoxon statistical test was used to assay social novelty preference ( $\#P < 0.05$ ). p110 $\alpha^{flax/flax}$ : vehicle,  $n = 13$ ; p110 $\alpha^{nKO}$ ,  $n = 14$ . p110 $\beta^{flax/flax}$ : vehicle,  $n = 13$ ; p110 $\beta^{nKO}$ ,  $n = 14$ .

In addition, this study helps to clarify previously conflicting evidence for pre- or postsynaptic roles of PI3K during synaptic plasticity by establishing different loci of action for the different PI3K isoforms. We believe that this knowledge will be key to (i) understand the molecular mechanisms mediating the multiple actions of PI3K and (ii) define specific potential targets for pathological alterations of the PI3K/PTEN pathway, in cases such as autism, schizophrenia, or different forms of intellectual disability (6, 50–53).

We show here that genetic deletion of p110 $\alpha$  has a most profound effect disrupting neuronal and synaptic architecture. Using independent electrophysiological and morphological approaches, we report a marked decrease in neuron size, loss of dendritic complexity, and reduced number of synapses in p110 $\alpha^{\text{nKO}}$  neurons. This combined loss of dendritic length and synapse number is likely responsible for the reduced basal transmission in these neurons and the loss of cytoskeletal and synaptic proteins observed in the proteomic analysis. It is interesting that the size of the remaining synapses in p110 $\alpha^{\text{nKO}}$  neurons was significantly larger than in control neurons. This effect could be a consequence of a preferential loss of small synapses, or, alternatively, it may reflect a compensatory mechanism to preserve a certain level of synaptic drive in the face of a marked reduction in synapse number. The latter interpretation seems more likely, as the increase in synapse size was observed throughout the whole distribution of synapses, including large synapses [for example, the maximum area of the spine head, postsynaptic density (PSD) length, and PSD thickness all increased roughly by 50% in p110 $\alpha^{\text{nKO}}$  neurons]. Incidentally, this result would also be consistent with the impairment we observed in NMDAR-dependent LTP since larger synapses in p110 $\alpha^{\text{nKO}}$  neurons may be less plastic if they cannot be further potentiated. This interpretation is also backed-up by the increase in the levels of phosphorylated GluA1 receptors and cofilin. In addition, neurons were fully mature (1-month-old mice) when the genetic manipulation was executed. Therefore, these results imply that continuous PI3K activity provided by p110 $\alpha$  is necessary for the maintenance of these dendritic and synaptic structures.

In the case of the p110 $\beta$ , we have found a dual role depending on the synaptic compartment. Thus, at the postsynaptic terminal, p110 $\beta$  contributes to NMDAR-dependent LTP, together with p110 $\alpha$ . In addition, at the presynaptic terminal, p110 $\beta$  specifically limits glutamate release and mediates mGluR-LTD. These results fit previous observations linking increased p110 $\beta$  expression and enhanced mGluR-dependent LTD in the pathophysiology of Fragile X syndrome (19, 54, 55). Nevertheless, our results provide further mechanistic information on mGluR-LTD and its locus of expression. Both presynaptic reduction in glutamate release (56–60) and postsynaptic removal of AMPARs (61–63) have been shown to occur during mGluR-LTD. Both types of mechanisms for synaptic depression are possibly concurrent, and their prevalence may change during postnatal development (64). It is also well established that PI3K activity is required for synaptic depression during mGluR-LTD (17–19). The insight we are providing here is that the involvement of PI3K in this form of plasticity is exclusively presynaptic (for CA3-to-CA1 synapses), is mediated by p110 $\beta$ , and is caused by a sustained decrease in neurotransmitter release. Further work will be required to determine how p110 $\beta$  regulates presynaptic glutamate release. This regulation may occur at the level of vesicle exocytosis. Thus, plasma membrane phosphatidylinositol 4,5-bisphosphate (PIP<sub>2</sub>) (the substrate for PIP<sub>3</sub> synthesis by PI3K) has

been shown to be essential for secretion in hippocampal neurons, and increasing levels of this phosphoinositide have been observed upon electrical stimulation (65). Therefore, p110 $\beta$  may inhibit neurotransmitter release by reducing PIP<sub>2</sub> levels at the presynaptic membrane. Pharmacological inhibition of PI3K with LY294002 elicits a transient increase in both PIP<sub>2</sub> and exocytosis in chromaffin cells, implying that controlling PIP<sub>2</sub> levels on the plasma membrane could directly regulate exocytosis (66). On the other hand, p110 $\beta$  has previously been shown to promote autophagy (67) through its connection with the endocytic effector Rab5 (68). This mechanism may also link with presynaptic function, as neuronal autophagy reduces presynaptic release by limiting axonal endoplasmic reticulum calcium stores (69). A reduction in neuronal autophagy and protein turnover may also explain the accumulation of presynaptic vesicles (electron microscopy) and up-regulation of presynaptic proteins (proteomics) we have observed in the absence of p110 $\beta$ . Irrespective of the detailed mechanisms, these results have revealed a distinct molecular specialization of PI3K synaptic activities, with p110 $\alpha$  in charge of postsynaptic structural maintenance and p110 $\beta$  limiting presynaptic vesicle release. To note, these specialized functions are described for excitatory CA3 to CA1 synapses. We cannot rule out that these PI3K isoforms play different roles in inhibitory neurons. Alternatively, it is also worth considering that similar molecular actions may result in different functional outcomes if the presynaptic and postsynaptic parameters of the neuron are different, as it is the case across multiple neuronal types.

Dysfunctions in neuronal communication are widely considered the underlying cause of many psychiatric and neurological diseases. The distinct but partially overlapping functions of p110 $\alpha$  and p110 $\beta$  described here allow us to underscore specific cognitive alterations associated with different molecular and synaptic changes. Genetic deletion of either p110 $\alpha$  or p110 $\beta$  isoform in the hippocampus produced hyperlocomotion (open field test). However, these phenotypes were qualitatively different with respect to the habituation component. Thus, p110 $\beta^{\text{nKO}}$  mice were not able to habituate to the novel environment in the time window we monitored. This lack of habituation may also be related to the failure to discriminate between novel and familiar objects in p110 $\beta^{\text{nKO}}$  mice (NORT). mGluR-LTD has been linked to sensory adaptation and novelty recognition (70), brain processes that are thought to be defective in neuropsychiatric disorders (71). We now propose that these deficits may be related to a failure to depress presynaptic function in the absence of p110 $\beta$ . In contrast, the hyperlocomotion and enhanced object exploration of p110 $\alpha^{\text{nKO}}$  mice did not preclude habituation to the novel environment and conversely resulted in enhanced novel object discrimination. In a sense, it is remarkable that behavioral performance was fairly preserved in these memory tests (NOR and NOL) despite the profound reduction in synaptic connectivity observed in these animals. Other behavioral aspects were similarly impaired in p110 $\alpha^{\text{nKO}}$  and p110 $\beta^{\text{nKO}}$ , such as working memory (Y-maze test) and social interactions (both social recognition and social novelty). It is tempting to speculate that these deficits may be related to the impairment of LTP, which was observed in the absence of either p110 $\alpha$  or p110 $\beta$ .

In summary, this work provides a genetic dissection of the molecular specialization of the PI3K pathway for the control of morphological and functional properties of neurons, as well as for proper synaptic communication in the mature brain. This specialization may be relevant for cognitive functions in the context of

neurodevelopmental and psychiatric diseases and could pave the way for new therapeutic strategies in these neurological disorders.

## MATERIALS AND METHODS

### General experimental design

The objective of this study is to analyze the role of p110 $\alpha$  and p110 $\beta$  in specific neuronal and cognitive functions. To this end, we have deleted the corresponding gene from p110 $\alpha^{lox/lox}$  or p110 $\beta^{lox/lox}$  transgenic mice by expressing the *Cre* recombinase in hippocampal neurons of adult animals using AAVs. One month after infection, animals are subject to behavioral assays, and acute hippocampal slices are prepared for electrophysiological, biochemical, and microscopy experiments.

### Reagents

DL-AP5 and picrotoxin were purchased from Sigma-Aldrich. PI3K isoform-specific inhibitors A66, TGX221, and CAL101 were purchased from APExBio. The antibody against p110 $\alpha$  was generated in M.G.'s laboratory. Other primary antibodies were GluA1 (Abcam, ab31232), p110 $\beta$  (Abcam, ab151549), glyceraldehyde-3-phosphate dehydrogenase (Abcam, ab8245), pAKT(Thr<sup>308</sup>) (Cell Signaling Technology, 2965), pAKT(Ser<sup>473</sup>) (Cell Signaling Technology, 4060), tAKT (Cell Signaling Technology, 9272 and 2920), mGluR5 (Millipore, AB5675), actin (Millipore, MAB1501R), GluA2 (NeuroMab, 75-002), PSD95 (Thermo Fisher Scientific, MA1-046), mCherry (GeneTex, GTX59788), SAP102 (Stressgen, VAM-PS006), CaMKII (Sigma-Aldrich, c6974), GluN1 (Millipore, 05-432), GluN2A (Millipore, 07-632), and GluN2B (NeuroMab, 75-097).

### Proteomics

Three mice for each condition (C57/BL6, p110 $\alpha^{lox/lox}$ , and p110 $\beta^{lox/lox}$ , infected in vivo with the AAV5-CaMKII-Cre-mCherry virus) were anesthetized and quickly decapitated once they were unresponsive to tail and foot pinches. The brains were rapidly removed and submerged in Ca<sup>2+</sup>-free ice-cold dissection solution [10 mM D-glucose, 4 mM KCl, 26 mM NaHCO<sub>3</sub>, 233.7 mM sucrose, 5 mM MgCl<sub>2</sub>, and 0.001% (w/v) phenol red as a pH indicator] previously saturated with carbogen (5% CO<sub>2</sub> and 95% O<sub>2</sub>). Then, hippocampi were dissected and briefly washed on 1 $\times$  ice-cold phosphate-buffered saline (137 mM NaCl, 2.68 mM KCl, 8.1 mM Na<sub>2</sub>HPO<sub>4</sub>, and 1.47 mM KH<sub>2</sub>PO<sub>4</sub> with pH adjusted to 7.4) containing protease and phosphatase inhibitor cocktails (cOmplete Mini EDTA-free and phosSTOP, Roche) before being coarsely homogenized by cutting the tissue with sharp scissors, transferred to 2-ml vials pre-filled with 200- $\mu$ m zirconium beads (SPEX SamplePrep, 2302-200AW), and snap-frozen in dry ice. Hippocampus protein extracts samples were prepared in lysis buffer [50 mM tris-HCl-2% SDS (pH 8.5) and 10 mM tris-(2-carboxyethyl)phosphine] containing protease and phosphatase inhibitor cocktails (cOmplete Mini EDTA-free and phosSTOP, Roche). Peptides were quantified using TMT isobaric labeling, and labeled peptides were analyzed by liquid chromatography tandem mass spectrometry using a C-18 reversed-phase nano-column coupled to an Orbitrap Q Exactive HF mass spectrometer (Thermo Fisher Scientific) as described (72). For peptide identification, all spectra were analyzed with Proteome Discoverer (version 2.1.0.81, Thermo Fisher Scientific) using SEQUEST-HT. For database searching at the UniProt mouse

database (September 2018; 53,780 entries), the parameters were selected as follows: trypsin digestion with two maximum missed cleavage sites, precursor and fragment mass tolerances of 2 and 0.02 Da, respectively, carbamidomethyl cysteine and TMT modifications at N terminus and Lys residues as fixed modifications, and methionine oxidation and Ser, Thr, and Tyr phosphorylation as dynamic modifications. Quantification of identified peptides was performed using the probability ratio method (73), and false discovery rate (FDR) was calculated using inverted databases and the refined method (74), with an additional filtering for a precursor mass tolerance of 15 parts per million (75). Statistical analysis of quantitative data for differential protein quantitation was performed with the in-house software SanXoT (76) using the WSPP statistical model previously described (77). In this model, protein and peptide log<sub>2</sub> ratios are expressed as standardized variables, i.e., in units of SD according to their estimated variances (Zq values for protein quantification). Differences in protein abundance were estimated by the comparison of the compared groups' Zq. A cutoff of  $\pm 1.2$  or higher for Zq values and a  $P < 0.05$  was used for the statistically significant identification of DEPs between the three experimental conditions. For functional analysis of the quantified proteins, identification of coordinated proteome changes and functional categories were performed using the Systems Biology Triangle algorithm (78) for the analysis of coordinated protein responses in high-throughput quantitative proteomics experiments. Posterior bioinformatic analysis was performed using the web-based tool G-profiler (Benjamini-Hochberg FDR correction threshold of 0.01) and RStudio with custom-made scripts using the packages: PCAtools v 2.1.22, pheatmap v 1.0.12, and corrplot v0.84. Principal components analysis and unsupervised hierarchical clustering from the total proteome were used to visualize sample clustering and variability.

### Animals and ethics statement

For the organotypic hippocampal cultured slices, we used Wistar rats of both genders. These animals were housed in standard cages with ad libitum access to food and water under a 12:12 hour dark-light cycle in humidity- and temperature-controlled rooms. The rest of the experiments were performed using adult mice (6 to 8 months). All mice used were housed in standard cages (maximum of five animals per cage) in humidity- and temperature-controlled rooms. Autoventilated racks contained individually ventilated animal cages with absolute filters. Irradiated standard safe diet and autoclaved water were available ad libitum.

p110 $\alpha^{lox/lox}$  is a transgenic mouse line with the 18th and 19th exons of the *PIK3CA* gene flanked by two LoxP sequences. p110 $\beta^{lox/lox}$  is a transgenic mouse line with the 21st and 22nd exons of the *PIK3CB* gene flanked by two LoxP sequences. These mice were contributed by M.G.'s laboratory. Transgenesis procedures to generate these mice were previously described (39, 79). Their genetic background is C57BL/6J (the Jackson Laboratory). Genotyping was carried out by polymerase chain reaction using the following primers: p110 $\alpha^{lox/lox}$ , GGATGCGGTCTTTATTGTC (FE1) and TGGCATGCTGCCAATTG (FE4); p110 $\beta^{lox/lox}$ , AGTGAACGCTATGCATCACACCAGC (b3) and AAGTACAAA-CATCCAAGCAA (b98). All biosafety procedures and animal experimental protocols were approved by the Ethical Committee from the Consejo Superior de Investigaciones Científicas, in strict accordance with Spanish (RD 53/2013, 32/2007) and E.U.

guidelines set out in the European Community Council Directives (2010/63/EU and 86/609/EEC).

### Stereotaxic in vivo microinjections of AAV and Sindbis virus

AAV5-CaMKII-Cre-mCherry virus (serotype 5,  $5.8 \times 10^{12}$  viral particles/ml, Gene Therapy Vector Core at the University of North Carolina) was delivered to the hippocampus through two bilateral injections (650 nl each, 120 nl/min) in the dorsal [from bregma: anterior-posterior (AP),  $-1.8$  mm; medial-lateral (ML),  $\pm 1.3$  mm; dorsal-ventral (DV),  $-1.7$  mm] and ventral (AP,  $-2.8$  mm; ML,  $\pm 2.4$  mm; DV,  $-2$  mm) regions. The 3- to 4-month-old animals were placed in the stereotaxic frame (Harvard Apparatus) over a heating pad and immobilized using blunt ear holders. Anesthesia was initiated and maintained by inhalation of 2% isoflurane in oxygen. Viral solution was infused using a Hamilton Neurosyringe (65460-02) inserted through small holes drilled into the skull and coupled to a micropump (120 nl/min; Quintessential Stereotaxic Injector, Stoelting, 53311). After the infusion, the syringe was kept in place for 5 min and slowly withdrawn. After the closure of the wound, the animals received analgesia by subcutaneous injection of meloxicam (5 mg/kg of dose). For CA1-specific injections, we used the same protocol, but we performed three bilateral injections (50 nl each, 50 nl/min): rostral (AP,  $-1.8$  mm; ML,  $\pm 1.3$  mm; DV,  $-1.6$  mm), medial (AP,  $-2.3$  mm; ML,  $\pm 1.7$  mm; DV,  $-1.7$  mm), and caudal (AP,  $-2.8$  mm; ML,  $\pm 2.6$  mm; DV,  $-2$  mm). The accuracy of the infection was confirmed after 1 month by immunofluorescence using the expression of mCherry as the reporter. For neuron morphology experiments, injected mice were subjected to a second round of in vivo injections using the previous parameters to inject Sindbis viruses expressing GFP. Four weeks after infection, we observed Cre-expressing cells, which were distributed along the entire hippocampus. The rate of infection, as evaluated by colocalization with neuronal markers was  $89 \pm 5.2\%$  ( $N = 5$ ) (38).

### Behavior

#### Open field test

This test was used to evaluate general locomotor activity and as a habituation phase to NOLT and NORT. Mice were placed individually in the center of an acrylic box (40 cm by 40 cm by 40 cm) with white opaque walls at ground level. The animals were allowed to explore the arena for 5 min while being recorded. Their behavior was tracked using ANY-maze software.

#### NOLT, NORT, and reexposure test

Assays were performed on 3- to 4-month-old mice 24 hours after the open field test, which was used as habituation phase for NOLT, NORT, and reexposure. In the first phase of the NORT, mice were placed in the open field arena containing two identical objects in terms of color, texture, and shape on two adjacent corners of the arena. Mice were allowed to explore the objects for 7 min while being recorded. In the test phase of the NORT (3 hours later), one of the objects was switched for another one of similar dimensions and texture but different in color and shape. Then, mice were allowed to explore both objects for 7 min. The objects used were a pair of orange triangular prisms and a pair of blue pyramids. Both groups of objects were randomly assigned as familiar or novel among the subjects to ensure that they showed no preference for any of them. In the NOLT, the objects were a pair of white square prisms identical in shape, dimensions, and

texture. During the familiarization phase, both objects were placed in two adjacent corners. In the test phase of the NOLT, the location of one of the objects was changed to the opposite corner. In the reexposure testing, after habituating in an empty box on day 1, mice were exposed to two novel objects on the following day (training) and then reexposed to the same objects 3 hours later (reexposure). Data were expressed as a percentage of reexploration ("reexposure") relative to the initial exploration time (during "training"). In the NORT, NOLT, and reexposure, the arena and the objects were cleaned thoroughly with 70% ethanol in between phases to eliminate any olfactory cues. Behavior was recorded from a camera located above the arena, and the analysis was performed manually in time segments of 1 min by an experimenter blinded to the treatment using the ANY-maze software. Exploration of the objects was defined as close contact sniffing (with the head pointed toward the object and within 2 cm of the object). We then calculated a discrimination index as the time spent exploring the relocated or novel object divided by the time exploring both objects.

#### Social interaction and social memory test

This task is used to evaluate social interaction in mice and their preference to establish social contact. The social memory task also relies on the mice's innate preference for novelty. For this task, we used a three-chamber acrylic box with clear dividing walls that have a hole to give the testing mouse access to each chamber. This test consisted of three phases. On the first phase, wire cages were placed on the two outermost chambers allowing visual, auditory, olfactory, and minimal touch interaction. Mice were allowed to explore the arena for 5 min. For the second phase, the social interaction task was performed 24 hours later. An unfamiliar mouse was placed under the wire cage of one of the chambers (gender- and age-paired), and an inanimate object was placed on the opposite cage in an identical configuration. The unfamiliar mice had been habituated to the wire cage for intervals of 15 min before the test. In the testing phase, the subject mouse was placed in the center chamber and allowed to freely explore all three chambers for 7 min. The test mouse was removed, and the third phase was immediately started after cleaning the arena and the wire cages thoroughly with ethanol 70% to eliminate any olfactory cues. For the third phase, the social memory task, the inanimate object was replaced by another unfamiliar mouse, and the test was performed exactly as in the second phase. Behavior was recorded from a camera located above the test box, and analysis was performed manually in time segments of 1 min. We measured number of visits to each chamber, time spent on each chamber, and exploration. Exploration of the targets was defined as close contact sniffing of the wire cage (with the head pointed toward the cage). Sitting or standing time on the wire cages was not quantified as exploration. We also calculated the discrimination index as the time exploring the subject versus the time exploring the subject and the object in the first phase and the time exploring the new subject versus the new and the familiar.

#### Elevated plus maze test

This test is widely accepted to test anxiety-like behavior (80). The apparatus consists of a plus-shaped maze elevated 45 cm from the ground and has two opposite positioned open arms with railing (5 cm by 29.5 cm by 0.3 cm), two opposite closed arms (5 cm by 29.5 cm by 15 cm), and a center area (5 cm by 5 cm). Mice were tested in a single trial by being placed in the center area and recorded from above for 5 min. To eliminate odor cues, the maze was thoroughly cleaned with 70% ethanol and allowed to dry in between subjects.



The analysis was performed in time segments of 1 min both manually and using the ANY-maze software.

#### **Y-maze test**

The Y-maze test was performed to quantify spontaneous alternation and assess deficits or enhancements on spatial working memory. The apparatus consists of a Y-shaped maze with three identical enclosed arms. Each arm was assigned a letter from A to C. To perform the test, we placed each mouse in the center of the maze and recorded a single trial of 5 min from above. To eliminate odor cues, the maze was thoroughly cleaned with 70% ethanol and allowed to dry in between subjects. The sequence of arm entrance was recorded manually, and an alternation is considered a consecutive entrance in all three arms. The spontaneous alternation percentage was calculated using the following equation: % spontaneous alternation = (number of alternations)  $\times$  100 / (total number of arm entrances – 2).

#### **Hippocampal slice preparation**

##### **Organotypic cultured hippocampal slices**

Organotypic cultures were established from rat pups (5 to 7 days old) according to previously described procedures. Animals were anesthetized and quickly decapitated once they were unresponsive to tail and foot pinches. Whole brains were extracted and immersed in ice-cold dissection solution [10 mM glucose, 4 mM KCl, 26 mM NaHCO<sub>3</sub>, 233.7 mM sucrose, 5 mM MgCl<sub>2</sub>, and 1 mM CaCl<sub>2</sub> with 0.001% (w/v) phenol red as a pH indicator], previously saturated with carbogen (5% CO<sub>2</sub> and 95% O<sub>2</sub>). Hippocampi were dissected under sterile conditions and placed over a tissue slicer (Stoelting Europe, 51425) to obtain 400- $\mu$ m-thick slices. These slices were then transferred to porous nitrocellulose membranes (Merck Millipore, PICMORG50) on culture medium [0.8% (w/v) minimum essential medium powder, 20% (v/v) horse serum, 1 mM L-glutamine, 1 mM CaCl<sub>2</sub>, 2 mM MgSO<sub>4</sub>, insulin (1 mg/liter), 0.0012% (v/v) ascorbic acid, 30 mM Hepes, 13 mM D-glucose, and 5.2 mM NaHCO<sub>3</sub>] and maintained at 35.5°C and 5% CO<sub>2</sub> for a minimum of 7 days and up to 15 days. The culture medium was replaced every 2 to 3 days. These slices were recorded in artificial cerebrospinal fluid (aCSF) containing 119 mM NaCl, 2.5 mM KCl, 1 mM NaH<sub>2</sub>PO<sub>4</sub>, 11 mM glucose, 26 mM NaHCO<sub>3</sub>, 4 mM MgCl<sub>2</sub>, 4 mM CaCl<sub>2</sub>, and osmolarity adjusted to 290  $\pm$  5 mOsm. For electrophysiological experiments in the presence of pharmacological inhibitors, 0.01% dimethyl sulfoxide (DMSO; vehicle), 2.5  $\mu$ M A66, or 0.5  $\mu$ M TGX221 in 0.01% DMSO were added to the culture medium for overnight treatment and reapplied 2 hours before the experiment. These inhibitors were also added to the aCSF during the recordings at the same concentrations. The identity of the pharmacological inhibitors was coded so that the experiments could be performed blindly.

##### **Acute slices for field recordings**

Acute hippocampal slices were obtained from 4-month-old mice of both genders. Animals were anesthetized and quickly decapitated once they were unresponsive to tail and foot pinches. The brains were rapidly removed and submerged in Ca<sup>2+</sup>-free ice-cold dissection solution (10 mM D-glucose, 4 mM KCl, 26 mM NaHCO<sub>3</sub>, 233.7 mM sucrose, 5 mM MgCl<sub>2</sub>, and 0.001% (w/v) phenol red as a pH indicator) previously saturated with carbogen (5% CO<sub>2</sub> and 95% O<sub>2</sub>). Coronal slices (350  $\mu$ m) were obtained by cutting the brain in the same solution with a vibratome (Leica, VT1200S) and left in carbogen-gassed aCSF (119 mM NaCl, 2.5 mM KCl, 1 mM

NaH<sub>2</sub>PO<sub>4</sub>, 26 mM NaHCO<sub>3</sub>, 11 mM glucose, 1.2 mM MgCl<sub>2</sub>, 2.5 mM CaCl<sub>2</sub>, and osmolarity adjusted to 290 mOsm) for 1 hour at 32°C to recover. Past that time, the slices were maintained at 25°C, and the recordings were performed in the same aCSF solution used for recovery.

##### **Acute slices for whole-cell recordings**

Slices were obtained as previously described (38). Briefly, animals were anesthetized, and once they became unresponsive to foot and tail pinches, they were intracardially perfused with cold-choline aCSF (92 mM choline chloride, 2.5 mM KCl, 1.2 mM NaH<sub>2</sub>PO<sub>4</sub>, 30 mM NaHCO<sub>3</sub>, 20 mM Hepes, 25 mM glucose, 5 mM sodium ascorbate, 2 mM thiourea, 3 mM sodium pyruvate, 10 mM MgSO<sub>4</sub>, 0.5 mM CaCl<sub>2</sub>, and osmolarity adjusted to 305  $\pm$  5 mOsm and pH to 7.35). The brains were rapidly removed and placed in cold-choline aCSF. Coronal slices (350  $\mu$ m) were obtained by cutting the brain in cold-choline aCSF. Then, the slices were recovered for <10 min in warm-choline aCSF (32°C) and then transferred to Hepes holding aCSF (92 mM NaCl, 2.5 mM KCl, 1.2 mM NaH<sub>2</sub>PO<sub>4</sub>, 30 mM NaHCO<sub>3</sub>, 20 mM Hepes, 25 mM glucose, 5 mM sodium ascorbate, 2 mM thiourea, 3 mM sodium pyruvate, 2 mM MgSO<sub>4</sub>, 2 mM CaCl<sub>2</sub>, and osmolarity adjusted to 305  $\pm$  5 mOsm and pH to 7.35) for 1 hour at 32°C. Past that time, the slices were maintained in recording aCSF (119 mM NaCl, 2.5 mM KCl, 1.2 mM NaH<sub>2</sub>PO<sub>4</sub>, 24 mM NaHCO<sub>3</sub>, 12.5 mM glucose, 2 mM MgSO<sub>4</sub>, 2 mM CaCl<sub>2</sub>, osmolarity adjusted to 305  $\pm$  5 mOsm and pH to 7.35) at 30°C, and the electrophysiological recordings were performed in the same solution.

#### **Electrophysiology**

Excitatory postsynaptic currents (EPSCs) and fEPSPs were recorded from CA1 pyramidal neurons with glass recording electrodes while stimulating Schaffer collateral fibers to evoke synaptic responses. During the recordings, the slices were placed in an immersion chamber constantly perfused with aCSF. The aCSF was continuously gassed with 5% CO<sub>2</sub> and 95% O<sub>2</sub>, and its temperature was closely monitored and maintained at 29°C for whole-cell recordings and at 25°C for all field recording experiments except for mGluR-LTD experiments, which were performed at 30°C. For all experiments, aCSF was supplemented with 100  $\mu$ M picrotoxin to block  $\gamma$ -aminobutyric acid type A receptors. For mGluR-LTD, 100  $\mu$ M DL-AP5 was added to the aCSF to block NMDARs. Patch-clamp recording glass electrodes (4 to 8 MOhm) were composed of silver/silver chloride electrodes inserted in glass pipettes filled with intracellular solution (115 mM CsMeSO<sub>3</sub>, 20 mM CsCl, 10 mM Hepes, 2.5 mM MgCl<sub>2</sub>, 4 mM Na<sub>2</sub>-ATP, 0.4 mM Na-guanosine triphosphate, 10 mM sodium phosphocreatine, 0.6 mM EGTA, 10 mM lidocaine N-ethyl bromide, and pH adjusted to 7.25 and osmolarity to 290  $\pm$  5 mOsm). In the case of field recordings, glass pipettes (0.5 to 1 MOhm) were filled with the aCSF used as extracellular solution and placed in CA1 stratum radiatum.

AMPA-mediated responses were measured at –60 mV. NMDAR-mediated responses were measured at +40 mV at a point when AMPA-mediated responses had fully decayed (65 ms after stimulation). PPR experiments were performed with 50-ms interstimulus intervals. NMDAR-dependent LTP under whole-cell patch clamp was induced using a pairing protocol that consists of presynaptic stimulation at 3 Hz (300 pulses) coupled to postsynaptic depolarization to 0 mV. NMDAR-dependent LTP for field recordings was induced using a theta-burst protocol

composed of 10 trains of bursts (four pulses at 100 Hz with a 200-ms interval), and it was repeated for four cycles with 20-s intercycle interval. NMDAR-dependent LTD was induced using low-frequency (1 Hz, 900 pulses) presynaptic stimulation. mGluR-dependent LTD was induced using low-frequency (1 Hz, 900 pulses) presynaptic stimulation with paired pulses (50-ms interstimulus interval). Stimulation intensity was adjusted to 30% (for LTP and PPR) or 70% (for LTD) of the maximum response.

Data acquisition was carried out with MultiClamp 700 A/B amplifiers and pClamp software (Molecular Devices). Data analysis was performed using custom-made Excel (Microsoft) macros.

### Confocal fluorescence microscopy and morphometry

Mice were anesthetized by isoflurane inhalation and intracardially perfused with phosphate buffer (PB) to wash the vascular system before injecting the fixative [4% paraformaldehyde in 0.1 M PB (pH 7.4)]. Brains were postfixed overnight by immersion in the same fixative solution at 4°C and then sequentially dehydrated in solutions containing 15 and 30% sucrose in PB at 4°C. Brains were cut in 100- $\mu$ m coronal slices, stained with 4',6-diamidino-2-phenylindole (DAPI; 1  $\mu$ g/ml) for 5 min and mounted on adherent microscope slides (Thermo Fisher Scientific, 15438060) with ProLong Glass Antifade (Thermo Fisher Scientific, P-36982). Fluorescence images for dendrite morphology were acquired as Z-stacks with a confocal inverted microscope (Zeiss, LSM800) using a 25 $\times$  numerical aperture (NA) 0.8 Plan-Apochromat M27 oil immersion objective and 488- and 555-nm lasers. Z-stacks were reconstructed using Fiji v1.51 (average intensity projection), and the neuronal dendritic trees were two-dimensionally traced with the simple neurite tracer plug-in. The Sholl analysis was performed counting the number of intersections in 10- $\mu$ m intervals from the soma as well as the total basal and apical dendritic length. Images for spine morphology were acquired as Z-stacks using a 63 $\times$  NA 0.8 Plan-Apochromat M27 oil immersion objective and a 488-nm laser. For deconvolution purposes, spine morphology images were acquired under an optimal calculated zoom of 3 $\times$ , an XY pixel size of <43 nm, and a Z-step size of 130 nm. The stacks were processed after image acquisition with a three-dimensional deconvolution algorithm using Huygens software (Huygens 19.10, SVI). Spine density was defined as the number of spines divided by the corresponding dendritic length.

### Electron microscopy

Mice were anesthetized by isoflurane inhalation and intracardially perfused with PB to wash the vascular system before injecting the fixative [4% paraformaldehyde and 2% glutaraldehyde in 0.1 M PB (pH 7.4)]. Brains were left for 2 hours at room temperature and overnight at 4°C immersed in the same fixative solution. Coronal slices of 200  $\mu$ m were obtained and postfixed in a 2% solution of osmium tetroxide in 0.1 M PB (1.5 hours at room temperature). The slices were then washed and stained with 2% uranyl acetate in water (1 hour at room temperature in darkness), washed, dehydrated in increasing concentrations of ethanol, and embedded in Epon resin. Series of ultrathin sections of the CA1 region of the hippocampus were collected and mounted on single oval slot copper/palladium grids. The sections were imaged on a JEM-1400Flash transmission electron microscope (JEOL) coupled to a complementary metal-oxide semiconductor Oneview camera (Gatan). The stratum radiatum proximal to the stratum pyramidale

was imaged with a  $\times$ 8000 magnification, and the PSD size, length, and number of vesicles were measured manually using Fiji v1.51.

### Western blotting

Brains were extracted from four animals for each condition (control, p110 $\alpha^{\text{NKO}}$ , and p110 $\beta^{\text{NKO}}$ ). Hippocampi were dissected and homogenized in a glass-teflon potter on ice-cold buffer containing 20 mM Hepes, 0.1% NP-40, cOmplete mini EDTA-free, and phosSTOP and centrifuged at 13,000g for 10 min at 4°C. The supernatant processed on SDS-polyacrylamide gel electrophoresis and transferred to a polyvinylidene difluoride membrane (Immoblot-P Millipore). After membrane blocking for 1 hour in 5% skim milk in Tris-buffered saline with 0.1% Tween 20, primary antibodies were incubated overnight at 4°C in blocking solution. Membranes were washed in TBST and incubated for 1 hour in the corresponding secondary antibodies (peroxidase-conjugated anti-rabbit or anti-mouse; the Jackson ImmunoResearch, 711-035-152 and 715-035-151). Detection was carried out by chemiluminescence (Immobilon Western, Millipore) using ImageQuant LAS 4000 mini biomolecular imager.

### Statistical analyses

Unless otherwise indicated, results were represented as means  $\pm$  SEM. For pairwise comparisons, *P* values were calculated according to two-tailed Mann-Whitney tests (for unpaired data) or Wilcoxon tests (for paired data). For multiple comparisons, we used two-way repeated-measures analysis of variance (ANOVA), followed by Bonferroni's post hoc analysis. The values for *N*, *P*, and the specific statistical test performed for each experiment are described in the corresponding figure legend. A complete report of the statistical analysis of the proteomics data can be found above in the "Proteomics" section and in data S1.

### Supplementary Materials

This PDF file includes:

Figs. S1 to S11

Other Supplementary Material for this manuscript includes the following:

Data S1

[View/request a protocol for this paper from Bio-protocol.](#)

### REFERENCES AND NOTES

1. T. V. P. Bliss, G. L. Collingridge, A synaptic model of memory: Long-term potentiation in the hippocampus. *Nature* **361**, 31–39 (1993).
2. S. J. Martin, P. D. Grimwood, R. G. M. Morris, Synaptic plasticity and memory: An evaluation of the hypothesis. *Annu. Rev. Neurosci.* **23**, 649–711 (2000).
3. S. Knafo, J. A. Esteban, Common pathways for growth and for plasticity. *Curr. Opin. Neurobiol.* **22**, 405–411 (2012).
4. K. L. Arendt, M. Royo, M. Fernández-Monreal, S. Knafo, C. N. Petrok, J. R. Martens, J. A. Esteban, PIP 3 controls synaptic function by maintaining AMPA receptor clustering at the postsynaptic membrane. *Nat. Neurosci.* **13**, 36–44 (2010).
5. S. Jurado, M. Benoist, A. Lario, S. Knafo, C. N. Petrok, J. A. Esteban, PTEN is recruited to the postsynaptic terminal for NMDA receptor-dependent long-term depression. *EMBO J.* **29**, 2827–2840 (2010).
6. S. Knafo, J. A. Esteban, PTEN: Local and global modulation of neuronal function in health and disease. *Trends Neurosci.* **40**, 83–91 (2017).
7. C. Sánchez-Puelles, M. Calleja-Felipe, A. Ouro, G. Bougama, A. Arroyo, I. Diez, A. Erramuzpe, J. Cortés, J. Martínez-Hernández, R. Luján, M. Navarrete, C. Venero, A. Chan, M. Morales,

- J. A. Esteban, S. Knafo, PTEN activity defines an axis for plasticity at cortico-amygdala synapses and influences social behavior. *Cereb. Cortex* **30**, 505–524 (2020).
8. K. Takeuchi, M. J. Gertner, J. Zhou, L. F. Parada, M. V. L. Bennett, R. S. Zukin, Dysregulation of synaptic plasticity precedes appearance of morphological defects in a Pten conditional knockout mouse model of autism. *Proc. Natl. Acad. Sci. U.S.A.* **110**, 4738–4743 (2013).
  9. P. J. Blair, J. Harvey, PTEN: A new player controlling structural and functional synaptic plasticity. *J. Physiol.* **590**, 1017–1017 (2012).
  10. M. M. Fraser, I. T. Bayazitov, S. S. Zakharenko, S. J. Baker, Phosphatase and tensin homolog, deleted on chromosome 10 deficiency in brain causes defects in synaptic structure, transmission and plasticity, and myelination abnormalities. *Neuroscience* **151**, 476–488 (2008).
  11. D. K. Chow, M. Groszer, M. Pribadi, M. Machnicki, S. T. Carmichael, X. Liu, J. T. Trachtenberg, Laminal and compartmental regulation of dendritic growth in mature cortex. *Nat. Neurosci.* **12**, 116–118 (2009).
  12. K. L. Arendt, M. Royo, M. Fernández-Monreal, S. Knafo, C. N. Petrok, J. R. Martens, J. A. Esteban, PI3K controls synaptic function by maintaining AMPA receptor clustering at the postsynaptic membrane. *Nat. Neurosci.* **13**, 36–44 (2010).
  13. P. Opazo, A. M. Watabe, S. G. N. Grant, T. J. O'Dell, Phosphatidylinositol 3-kinase regulates the induction of long-term potentiation through extracellular signal-related kinase-independent mechanisms. *J. Neurosci.* **23**, 3679–3688 (2003).
  14. P. P. Sanna, M. Cammalleri, F. Bertoni, C. Simpson, R. Lutjens, F. E. Bloom, W. Francesconi, Phosphatidylinositol 3-kinase is required for the expression but not for the induction or the maintenance of long-term potentiation in the hippocampal CA1 region. *J. Neurosci.* **22**, 3359–3365 (2002).
  15. H. Y. Man, Q. Wang, W. Y. Lu, W. Ju, G. Ahmadian, L. Liu, S. D'Souza, T. P. Wong, C. Tachibiglou, J. Lu, L. E. Becker, L. Pei, F. Liu, M. P. Wymann, J. F. MacDonald, Y. T. Wang, Activation of PI3-kinase is required for AMPA receptor insertion during LTP of mEPSCs in cultured hippocampal neurons. *Neuron* **38**, 611–624 (2003).
  16. C. H. Lin, S. H. Yeh, C. H. Lin, K. T. Lu, T. H. Leu, W. C. Chang, P. W. Gean, A role for the PI-3 kinase signaling pathway in fear conditioning and synaptic plasticity in the amygdala. *Neuron* **31**, 841–851 (2001).
  17. L. Hou, E. Klann, Activation of the phosphoinositide 3-kinase-Akt-mammalian target of rapamycin signaling pathway is required for metabotropic glutamate receptor-dependent long-term depression. *J. Neurosci.* **24**, 6352–6361 (2004).
  18. W. B. Potter, T. Basu, K. J. O'Riordan, A. Kirchner, P. Rutecki, C. Burger, A. Roopra, Reduced juvenile long-term depression in tuberous sclerosis complex is mitigated in adults by compensatory recruitment of mGluR5 and Erk signaling. *PLOS Biol.* **11**, e1001627 (2013).
  19. C. Gross, A. Banerjee, D. Tiwari, F. Longo, A. R. White, A. G. Allen, L. M. Schroeder-Carter, J. C. Krzeski, N. A. Elsayed, R. Puckett, E. Klann, R. A. Rivero, S. L. Gourley, G. J. Bassell, Isoform-selective phosphoinositide 3-kinase inhibition ameliorates a broad range of fragile X syndrome-associated deficits in a mouse model. *Neuropsychopharmacology* **44**, 324–333 (2019).
  20. J. I. Kim, H. R. Lee, S. E. Sim, J. Baek, N. K. Yu, J. H. Choi, H. G. Ko, Y. S. Lee, S. W. Park, C. Kwak, S. J. Ahn, S. Y. Choi, H. Kim, K. H. Kim, P. H. Backx, C. A. Bradley, E. Kim, D. J. Kang, K. Lee, S. J. Kim, M. Zhuo, G. L. Collingridge, B. K. Kaang, PI3K $\gamma$  is required for NMDA receptor-dependent long-term depression and behavioral flexibility. *Nat. Neurosci.* **14**, 1447–1454 (2011).
  21. J. H. Choi, P. Park, G. C. Baek, S. E. Sim, S. J. J. Kang, Y. Lee, S. H. Ahn, C. S. Lim, Y. S. Lee, G. L. Collingridge, B. K. Kaang, Effects of PI3K $\gamma$  overexpression in the hippocampus on synaptic plasticity and spatial learning. *Mol. Brain* **7**, 78 (2014).
  22. V. L. Hood, C. Paterson, A. J. Law, PI3Kinase-p110 $\delta$  overexpression impairs dendritic morphogenesis and increases dendritic spine density. *Front. Mol. Neurosci.* **13**, 29 (2020).
  23. J. Jaworski, S. Spangler, D. P. Seeburg, C. C. Hoogenraad, M. Sheng, Control of dendritic arborization by the phosphoinositide-3'-kinase-Akt-mammalian target of rapamycin pathway. *J. Neurosci.* **25**, 11300–11312 (2005).
  24. V. Kumar, M. X. Zhang, M. W. Swank, J. Kunz, G. Y. Wu, Regulation of dendritic morphogenesis by Ras-PI3K-Akt-mTOR and Ras-MAPK signaling pathways. *J. Neurosci.* **25**, 11288–11299 (2005).
  25. A. Martín-Peña, A. Acebes, J. R. Rodríguez, A. Sorribes, G. G. De Polavieja, P. Fernández-Fúnez, A. Ferrús, Age-independent synaptogenesis by phosphoinositide 3 kinase. *J. Neurosci.* **26**, 10199–10208 (2006).
  26. G. Cuesto, L. Enriquez-Barreto, C. Caramés, M. Cantarero, X. Gasull, C. Sandi, A. Ferrús, Á. Acebes, M. Morales, Phosphoinositide-3-kinase activation controls synaptogenesis and spinogenesis in hippocampal neurons. *J. Neurosci.* **31**, 2721–2733 (2011).
  27. S. Jordán-Álvarez, W. Fouquet, S. J. Sigris, A. Acebes, Presynaptic PI3K activity triggers the formation of glutamate receptors at neuromuscular terminals of *Drosophila*. *J. Cell Sci.* **125**, 3621–3629 (2012).
  28. S. Jordán-Álvarez, E. Santana, S. Casas-Tintó, Á. Acebes, A. Ferrús, The equilibrium between antagonistic signaling pathways determines the number of synapses in *Drosophila*. *PLOS ONE* **12**, 3621–3629 (2017).
  29. K. E. Cosker, B. J. Eickholt, Phosphoinositide 3-kinase signalling events controlling axonal morphogenesis. *Biochem. Soc. Trans.* **35**, 207–210 (2007).
  30. L. C. Cantley, The phosphoinositide 3-kinase pathway. *Science* **296**, 1655–1657 (2002).
  31. B. Bilanges, Y. Posor, B. Vanhaesebroeck, PI3K isoforms in cell signalling and vesicle trafficking. *Nat. Rev. Mol. Cell Biol.* **20**, 515–534 (2019).
  32. B. Vanhaesebroeck, J. Guillermet-Guibert, M. Graupera, B. Bilanges, The emerging mechanisms of isoform-specific PI3K signalling. *Nat. Rev. Mol. Cell Biol.* **11**, 329–341 (2010).
  33. B. Vanhaesebroeck, M. J. Welham, K. Kotani, R. Stein, P. H. Warne, M. J. Zvelebil, K. Higashi, S. Volinia, J. Downward, M. D. Waterfield, p110 $\delta$ , A novel phosphoinositide 3-kinase in leukocytes. *Proc. Natl. Acad. Sci. U.S.A.* **94**, 4330–4335 (1997).
  34. I. Cuscó, A. Medrano, B. Gener, M. Vilardell, F. Gallastegui, O. Villa, E. González, B. Rodríguez-Santiago, E. Vilella, M. Del Campo, L. A. Pérez-Jurado, Autism-specific copy number variants further implicate the phosphatidylinositol signaling pathway and the glutamatergic synapse in the etiology of the disorder. *Hum. Mol. Genet.* **18**, 1795–1804 (2009).
  35. A. J. Law, Y. Wang, Y. Sei, P. O'Donnell, P. Piantadosi, F. Papaleo, R. E. Straub, W. Huang, C. J. Thomas, R. Vakkalanka, A. D. Besterman, B. K. Lipska, T. M. Hyde, P. J. Harrison, J. E. Kleinman, D. R. Weinberger, Neuregulin 1-ErbB4-PI3K signaling in schizophrenia and phosphoinositide 3-kinase-p110 $\delta$  inhibition as a potential therapeutic strategy. *Proc. Natl. Acad. Sci. U.S.A.* **109**, 12165–12170 (2012).
  36. L. Bi, I. Okabe, D. J. Bernard, A. Wynshaw-Boris, R. L. Nussbaum, Proliferative defect and embryonic lethality in mice homozygous for a deletion in the p110 $\alpha$  subunit of phosphoinositide 3-kinase. *J. Biol. Chem.* **274**, 10963–10968 (1999).
  37. L. Bi, I. Okabe, D. J. Bernard, R. L. Nussbaum, Early embryonic lethality in mice deficient in the p110 $\beta$  catalytic subunit of PI 3-kinase. *Mamm. Genome* **13**, 169–172 (2002).
  38. M. Navarrete, M. I. Cuartero, R. Palenzuela, J. E. Draffin, A. Konomi, I. Serra, S. Colié, S. Castaño-Castaño, M. T. Hasan, Á. R. Nebreda, J. A. Esteban, Astrocytic p38 $\alpha$  MAPK drives NMDA receptor-dependent long-term depression and modulates long-term memory. *Nat. Commun.* **10**, 2968 (2019).
  39. M. Graupera, J. Guillermet-Guibert, L. C. Foukas, L. K. Phng, R. J. Cain, A. Salpekar, W. Pearce, S. Meek, J. Millan, P. R. Cutillas, A. J. H. Smith, A. J. Ridley, C. Ruhrberg, H. Gerhardt, B. Vanhaesebroeck, Angiogenesis selectively requires the p110 $\alpha$  isoform of PI3K to control endothelial cell migration. *Nature* **453**, 662–666 (2008).
  40. S. Xie, J. Ni, J. R. McFaline-Figueroa, Y. Wang, R. T. Bronson, K. L. Ligon, P. Y. Wen, T. M. Roberts, J. J. Zhao, Divergent roles of PI3K isoforms in PTEN-deficient glioblastomas. *Cell Rep.* **32**, 108196 (2020).
  41. P. S. Kaeser, W. G. Regehr, The readily releasable pool of synaptic vesicles. *Curr. Opin. Neurobiol.* **43**, 63–70 (2017).
  42. S. Q. Ren, J. Z. Yan, X. Y. Zhang, Y. F. Bu, W. W. Pan, W. Yao, T. Tian, W. Lu, PKC $\lambda$  is critical in AMPA receptor phosphorylation and synaptic incorporation during LTP. *EMBO J.* **32**, 1365–1380 (2013).
  43. S. P. Jackson, S. M. Schoenwaelder, I. Goncalves, W. S. Nesbitt, C. L. Yap, C. E. Wright, V. Kenche, K. E. Anderson, S. M. Dopheide, Y. Yuan, S. A. Sturgeon, H. Prabakaran, P. E. Thompson, G. D. Smith, P. R. Shepherd, N. Daniele, S. Kulkarni, B. Abbott, D. Saylik, C. Jones, L. Lu, S. Giuliano, S. C. Hughan, J. A. Angus, A. D. Robertson, H. H. Salem, PI 3-kinase p110 $\beta$ : A new target for antithrombotic therapy. *Nat. Med.* **11**, 507–514 (2005).
  44. S. Jamieson, J. U. Flanagan, S. Kolekar, C. Buchanan, J. D. Kendall, W. J. Lee, G. W. Rewcastle, W. A. Denny, R. Singh, J. Dickson, B. C. Baguley, P. R. Shepherd, A drug targeting only p110 $\alpha$  can block phosphoinositide 3-kinase signalling and tumour growth in certain cell types. *Biochem. J.* **438**, 53–62 (2011).
  45. M. Fernández-Monreal, C. Sánchez-Castillo, J. A. Esteban, APPL1 gates long-term potentiation through its plekstrin homology domain. *J. Cell Sci.* **129**, 2793–2803 (2016).
  46. Y. Gutiérrez, S. López-García, A. Lario, S. Gutiérrez-Eisman, C. Delevoeye, J. A. Esteban, KIF13A drives AMPA receptor synaptic delivery for long-term potentiation via endosomal remodeling. *J. Cell Biol.* **220**, e202003183 (2021).
  47. A. Brachet, A. Lario, A. Fernández-Rodrigo, F. Heisler, Y. Gutiérrez, C. Lobo, M. Kneussel, J. Esteban, A kinesin 1-protrudin complex mediates AMPA receptor synaptic removal during long-term depression. *Cell Rep.* **36**, 109499 (2021).
  48. A. K. Kraeuter, P. C. Guest, Z. Sarnyai, The Y-maze for assessment of spatial working and reference memory in mice. *Methods Mol. Biol.* **1916**, 105–111 (2019).
  49. S. S. Moy, J. J. Nadler, A. Perez, R. P. Barbaro, J. M. Johns, T. R. Magnuson, J. Piven, J. N. Crawley, Sociability and preference for social novelty in five inbred strains: An approach to assess autistic-like behavior in mice. *Genes Brain Behav.* **3**, 287–302 (2004).
  50. M. G. Butler, M. J. Dazouki, X.-P. Zhou, Z. Talebizadeh, M. Brown, T. N. Takahashi, J. H. Miles, C. H. Wang, R. Stratton, R. Pilarski, C. Eng, Subset of individuals with autism spectrum disorders and extreme macrocephaly associated with germline PTEN tumour suppressor gene mutations. *J. Med. Genet.* **42**, 318–321 (2005).

51. H. O. Kalkman, The role of the phosphatidylinositol 3-kinase-protein kinase B pathway in schizophrenia. *Pharmacol. Ther.* **110**, 117–134 (2006).
52. S. C. Borrie, H. Brems, E. Legius, C. Bagni, Cognitive dysfunctions in intellectual disabilities: The contributions of the Ras-MAPK and PI3K-AKT-mTOR pathways. *Annu. Rev. Genomics Hum. Genet.* **18**, 115–142 (2017).
53. C. Gross, G. J. Bassell, Neuron-specific regulation of class I PI3K catalytic subunits and their dysfunction in brain disorders. *Front. Mol. Neurosci.* **7**, 12 (2014).
54. C. Gross, M. Nakamoto, X. Yao, C. B. Chan, S. Y. Yim, K. Ye, S. T. Warren, G. J. Bassell, Excess phosphoinositide 3-kinase subunit synthesis and activity as a novel therapeutic target in fragile X syndrome. *J. Neurosci.* **30**, 10624–10638 (2010).
55. C. Gross, N. Raj, G. Molinaro, A. G. Allen, A. J. Whyte, J. R. Gibson, K. M. Huber, S. L. Gourley, G. J. Bassell, Selective role of the catalytic PI3K subunit p110 $\beta$  in impaired higher order cognition in fragile X syndrome. *Cell Rep.* **11**, 681–688 (2015).
56. V. Y. Bolshakov, S. A. Siegelbaum, Postsynaptic induction and presynaptic expression of hippocampal long-term depression. *Science* **264**, 1148–1152 (1994).
57. S. H. R. Oliet, R. C. Malenka, R. A. Nicoll, Two distinct forms of long-term depression coexist in CA1 hippocampal pyramidal cells. *Neuron* **18**, 969–982 (1997).
58. S. S. Zakharenko, L. Zablow, S. A. Siegelbaum, Altered presynaptic vesicle release and cycling during mGluR-dependent LTD. *Neuron* **35**, 1099–1110 (2002).
59. A. M. Watabe, H. J. Carlisle, T. J. O'Dell, Postsynaptic induction and presynaptic expression of group 1 mGluR-dependent LTD in the hippocampal CA1 region. *J. Neurophysiol.* **87**, 1395–1403 (2002).
60. Y. Tan, N. Hori, D. O. Carpenter, The mechanism of presynaptic long-term depression mediated by group I metabotropic glutamate receptors. *Cell. Mol. Neurobiol.* **23**, 187–203 (2003).
61. M. Y. Xiao, Q. Zhou, R. A. Nicoll, Metabotropic glutamate receptor activation causes a rapid redistribution of AMPA receptors. *Neuropharmacology* **41**, 664–671 (2001).
62. E. M. Snyder, B. D. Philpot, K. M. Huber, X. Dong, J. R. Fallon, M. F. Bear, Internalization of ionotropic glutamate receptors in response to mGluR activation. *Nat. Neurosci.* **4**, 1079–1085 (2001).
63. M. W. Waung, B. E. Pfeiffer, E. D. Nosyreva, J. A. Ronesi, K. M. Huber, Rapid translation of Arc/Arg3.1 selectively mediates mGluR-dependent LTD through persistent increases in AMPAR endocytosis rate. *Neuron* **59**, 84–97 (2008).
64. E. D. Nosyreva, K. M. Huber, Developmental switch in synaptic mechanisms of hippocampal metabotropic glutamate receptor-dependent long-term depression. *J. Neurosci.* **25**, 2992–3001 (2005).
65. K. D. Micheva, R. W. Holz, S. J. Smith, Regulation of presynaptic phosphatidylinositol 4,5-bisphosphate by neuronal activity. *J. Cell Biol.* **154**, 355–368 (2001).
66. I. Milosevic, J. B. Sørensen, T. Lang, M. Krauss, G. Nagy, V. Haucke, R. Jahn, E. Neher, Plasmalemmal phosphatidylinositol-4,5-bisphosphate level regulates the releasable vesicle pool size in chromaffin cells. *J. Neurosci.* **25**, 2557–2565 (2005).
67. Z. Dou, M. Chattopadhyay, J. A. Pan, J. L. Guerriero, Y. P. Jiang, L. M. Ballou, Z. Yue, R. Z. Lin, W. X. Zong, The class IA phosphatidylinositol 3-kinase p110 $\beta$  subunit is a positive regulator of autophagy. *J. Cell Biol.* **191**, 827–843 (2010).
68. Z. Dou, J. A. Pan, H. A. Dbouk, L. M. Ballou, J. L. DeLeon, Y. Fan, J. S. Chen, Z. Liang, G. Li, J. M. Backer, R. Z. Lin, W. X. Zong, Class IA PI3K p110 $\beta$  subunit promotes autophagy through Rab5 small GTPase in response to growth factor limitation. *Mol. Cell* **50**, 29–42 (2013).
69. M. Kuijpers, G. Kochlamazashvili, A. Stumpf, D. Puchkov, A. Swaminathan, M. T. Lucht, E. Krause, T. Maritzen, D. Schmitz, V. Haucke, Neuronal autophagy regulates presynaptic neurotransmission by controlling the axonal endoplasmic reticulum. *Neuron* **109**, 299–313.e9 (2021).
70. C. Lüscher, K. M. Huber, Group 1 mGluR-dependent synaptic long-term depression: Mechanisms and implications for circuitry and disease. *Neuron* **65**, 445–459 (2010).
71. H. R. Monday, T. J. Younts, P. E. Castillo, Long-term plasticity of neurotransmitter release: Emerging mechanisms and contributions to brain function and disease. *Annu. Rev. Neurosci.* **41**, 299–322 (2018).
72. M. Bosch, M. Sánchez-Álvarez, A. Fajardo, R. Kapetanovic, B. Steiner, F. Dutra, L. Moreira, J. A. López, R. Campo, M. Mari, F. Morales-Paytuví, O. Tort, A. Gubern, R. M. Templin, J. E. B. Curson, N. Martel, C. Català, F. Lozano, F. Tebar, C. Enrich, J. Vázquez, M. A. Del Pozo, M. J. Sweet, P. T. Bozza, S. P. Gross, R. G. Parton, A. Pol, Mammalian lipid droplets are innate immune hubs integrating cell metabolism and host defense. *Science* **370**, eaay8085 (2020).
73. S. Martínez-Bartolomé, P. Navarro, F. Martín-Maroto, D. López-Ferrer, A. Ramos-Fernández, M. Villar, J. P. García-Ruiz, J. Vázquez, Properties of average score distributions of SEQUEST: The probability ratio method. *Mol. Cell. Proteomics* **7**, 1135–1145 (2008).
74. P. Navarro, J. Vazquez, A refined method to calculate false discovery rates for peptide identification using decoy databases. *J. Proteome Res.* **8**, 1792–1796 (2009).
75. E. Bonzon-Kulichenko, F. Garcia-Marques, M. Trevisan-Herraz, J. Vázquez, Revisiting peptide identification by high-accuracy mass spectrometry: Problems associated with the use of narrow mass precursor windows. *J. Proteome Res.* **14**, 700–710 (2015).
76. M. Trevisan-Herraz, N. Bagwan, F. García-Marqués, J. M. Rodríguez, I. Jorge, I. Ezkurdia, E. Bonzon-Kulichenko, J. Vázquez, SanXoT: A modular and versatile package for the quantitative analysis of high-throughput proteomics experiments. *Bioinformatics* **35**, 1594–1596 (2019).
77. P. Navarro, M. Trevisan-Herraz, E. Bonzon-Kulichenko, E. Núñez, P. Martínez-Acedo, D. Pérez-Hernández, I. Jorge, R. Mesa, E. Calvo, M. Carrascal, M. L. Hernández, F. García, J. A. Bárcena, K. Ashman, J. Abian, C. Gil, J. M. Redondo, J. Vázquez, General statistical framework for quantitative proteomics by stable isotope labeling. *J. Proteome Res.* **13**, 1234–1247 (2014).
78. F. García-Marqués, M. Trevisan-Herraz, S. Martínez-Martínez, E. Camafeita, I. Jorge, J. A. Lopez, N. Méndez-Barbero, S. Méndez-Ferrer, M. A. Del Pozo, B. Ibáñez, V. Andrés, F. Sánchez-Madrid, J. M. Redondo, E. Bonzon-Kulichenko, J. Vázquez, A novel systems-biology algorithm for the analysis of coordinated protein responses using quantitative proteomics. *Mol. Cell. Proteomics* **15**, 1740–1760 (2016).
79. J. Guillermet-Guibert, K. Bjorklof, A. Salpekar, C. Gonella, F. Ramadani, A. Bilancio, S. Meek, A. J. H. Smith, K. Okkenhaug, B. Vanhaesebroeck, The p110 $\beta$  isoform of phosphoinositide 3-kinase signals downstream of G protein-coupled receptors and is functionally redundant with p110 $\gamma$ . *Proc. Natl. Acad. Sci. U.S.A.* **105**, 8292–8297 (2008).
80. A. A. Wolf, C. A. Frye, The use of the elevated plus maze as an assay of anxiety-related behavior in rodents. *Nat. Protoc.* **2**, 322–328 (2007).

**Acknowledgments:** We thank the members of the Esteban laboratory for critical reading of the manuscript and the personnel at the fluorescence microscopy facility (SMOC) and the animal house of the CBM for expert technical assistance. We also thank the Genomics and Massive Sequencing facility of the CBM for assistance in the statistical analysis of the proteomic data. **Funding:** This work was supported by the Spanish Ministry of Science and Innovation grants SAF2017-86983-R and PID2020-117651RB (to J.A.E.), Spanish Ministry of Science and Innovation grants SAF2017-89116R-P (FEDER/EU) and PID2020-116184RB (to M.G.), Carlos III Institute of Health-Fondo de Investigación Sanitaria grant PRB3 (IPT17/0019-ISCIII-SGFEI/ERDF, ProteoRed) and CIBERCV (to J.A.L.), Spanish Ministry of Economy postdoctoral contract IJCI-2015-25507 (to M.I.C.), Marie Curie cofund UAM-UE (EU project 713366) Intertalentum Postdoctoral Program (to V.B.), and Spanish Ministry of Science and Innovation predoctoral contracts (to C.S.-C., A.F.-R., and S.L.-G.). The CNIC is supported by the Instituto de Salud Carlos III (ISCIII), the Ministerio de Ciencia e Innovación (MCIN), and the Pro CNIC Foundation, and is a Severo Ochoa Center of Excellence (grant CEX2020-001041-S funded by MICIN/AEI/10.13039/501100011033). **Author contributions:** Conceptualization and experimental design: C.S.-C., M.I.C., and J.A.E. Most experimental work and data analysis: C.S.-C. and M.I.C. Assistance with *in vivo* viral injections and behavioral assays: A.F.-R. Assistance with electrophysiological experiments: A.F.-R. and V.B. Assistance with some of the biochemical analyses: S.L.-G. and V.B. Mouse genotyping: R.J.-S. Proteomics and advice on analysis methodology: J.A.L. Provision of p110 $\alpha^{flox/flox}$  and p110 $\beta^{flox/flox}$  mice and advice on their analysis: M.G. Writing original draft and editing: C.S.-C., M.I.C., and J.A.E. **Competing interests:** The authors declare that they have no competing interests. **Data and materials availability:** All data needed to evaluate the conclusions in the paper are present in the paper and/or the Supplementary Materials.

Submitted 2 May 2022  
Accepted 25 October 2022  
Published 23 November 2022  
10.1126/sciadv.abq8109

## Functional specialization of different PI3K isoforms for the control of neuronal architecture, synaptic plasticity, and cognition

Carla Sánchez-CastilloMaría I. CuarteroAlba Fernández-RodrigoVÍctor BrizSergio López-GarcíaRaquel Jiménez-SánchezJuan A. LópezMariona GrauperaJosé A. Esteban

*Sci. Adv.*, 8 (47), eabq8109. • DOI: 10.1126/sciadv.abq8109

### View the article online

<https://www.science.org/doi/10.1126/sciadv.abq8109>

### Permissions

<https://www.science.org/help/reprints-and-permissions>

Use of this article is subject to the [Terms of service](#)